Electrical and Computer Engineering ETDs

Engineering ETDs

Spring 4-22-2018

Experimental Verification of A6 Magnetron with Permanent Magnet

Andrew J. Sandoval

Recommended Citation

Sandoval, Andrew J.. "Experimental Verification of A6 Magnetron with Permanent Magnet." (2018).
https://digitalrepository.unm.edu/ece_etds/400

Andrew J. Sandoval
Candidate

Electrical Engineering
Department

This thesis is approved, and it is acceptable in quality and form for publication:

Approved by the Thesis Committee:

Dr. Edl Schamiloglu , Chairperson

Dr. Christos Chrisodoulou

Dr. Ahmed Elfrgani

**EXPERIMENTAL VERIFICATION OF A6 MAGNETRON
WITH PERMANENT MAGNET**

by

ANDREW J. SANDOVAL

B.S. ELECTRICAL ENGINEERING

THESIS

Submitted in Partial Fulfillment of the
Requirements for the Degree of

Master of Science in Electrical Engineering

The University of New Mexico
Albuquerque, New Mexico

May, 2018

Dedications

I would like to dedicate this thesis to my parents and my sisters, Christina, Anjelica,

Emily, and Tiffany.

Acknowledgments

I would first like to thank my chair and advisor Dr. Edl Schamiloglu for accepting me as his student and for his continuous guidance in navigating me through my graduate academic career. Dr. Schamiloglu was always available for conversations regarding school, thesis work, and my forthcoming career. I would like to thank my other committee members Dr. Ahmed Elfrgani and Dr. Christos Christodoulou. I would also like to acknowledge and thank Dr. Sarita Prasad. At the beginning of this project she spent many hours of her personal time to help me understand the theoretical concepts of the experiment and how to use the simulation tools.

I would like to acknowledge and thank Daniel Reass and especially Dmitrii Andreev for all their hard work and many hours in helping me set-up and execute the experiment. Without their knowledge and support this thesis would not have been possible. Thank you to Khandakar Nusrat Islam for the encouragement and motivation during the writing process.

To John Kreger, Yeong-Jer "Jack" Chen and the other engineers and technicians of the Naval Surface Warfare Center- Dahlgren Division, thank you for your support during my visit to Dahlgren, Virginia.

A special thanks to Kenneth Leeson and Dinesh Mahadeo, my colleagues at Sandia National Laboratories, for the countless conversations regarding this thesis process.

Experimental Verification of A6 Magnetron with Permanent Magnet

By Andrew J. Sandoval

B.S., Electrical Engineering, University of New Mexico, 2012

M.S., Electrical Engineering, University of New Mexico, 2018

Abstract

A compact A6 relativistic magnetron with diffraction output using a transparent cathode, simple mode-converter, and a permanent magnet were simulated and tested at the University of New Mexico (UNM) for the Office of Naval Research. The standard compact MDO with a simple mode converter and transparent cathode radiates a TE_{11} mode axially through a cylindrical horn antenna. The magnetic field, essential for magnetron operation, is provided by a Neodymium Iron Boron (NeFeB) GradeN40M rare earth magnet. The permanent magnet eliminates the need for a pulsed magnet and accompanying circuit, significantly reducing the size of the system. A permanent magnetic field is also ideal for repetitive rate firing, which was demonstrated at the Naval Surface Warfare Center Dahlgren Division (NSWCDD) High Voltage Advanced Research (HIVAR) Laboratory in Dahlgren, Virginia.

An extensive sweep of input parameters was simulated using MAGIC, a three-dimensional particle-in-cell virtual prototyping tool to find the ideal operational parameters to be experimentally verified. A sweep of input voltages was completed experimentally using UNM's PULSERAD accelerator in order to compare and verify simulation results. The compact MDO with permanent magnet and transparent cathode were shipped to and assembled at the NSWCDD HIVAR Laboratory on their modulator and recommended input parameters from UNM's simulations and experimental verification were demonstrated. Results from the experimental set-up reproduced the qualitative behavior of the simulations and the simulated operating frequency of 2.5GHz was measured experimentally. The anticipated Gaussian radiation pattern from the

radiated TE_{11} mode was also experimentally verified by two ways, first by neon bulb grid array, and secondly by measuring the peak of the radiated microwave pulse relative to varying locations.

Table of Contents

Chapter 1: Introduction

1. Introduction

The objective of this study is to simulate, assemble, and experimentally verify simulation results of an A6 magnetron with a permanent magnet and transparent cathode. Chapter 1 will outline the history of magnetrons and high-power microwaves (HPMs), review previous work performed with A6 magnetrons that uses axial extraction and transparent cathodes, and review similar work performed at other universities.

1.1 History of Magnetrons and High-Power Microwaves

A magnetron is an HPM source that generates microwaves by means of electrons interacting with a magnetic field passing around a series of open cavities. In typical magnetrons a cathode is surrounded by the cylindrical anode which typically has an even number of open cavities arranged azimuthally around the cathode. The relativistic magnetron is a higher voltage, higher current version of the conventional magnetron where "relativistic voltages" are needed to produce higher currents [1]. These relativistic voltages are provided to the magnetron by pulsed power systems, which provide high peak power and power density to the load.

The advent of the magnetron as the microwave source that we know today is the product of several engineering breakthroughs in the field of electromagnetics. After receiving his doctorate in physics from Yale in 1909, Dr. Albert Wallace Hull was offered a position at General Electric Research Labs in 1913. Hull was originally assigned to work on various electronic tubes, one of which was the Kenotron. A Kenotron is a vacuum tube diode rectifier. In Hull's work with Kenotrons he reports having been able to construct a direct-current power source using a Kenotron that would supply 5 kW at any voltage between 10 and 100 kV [2]. Research with Kenotrons eventually led to the advent of the Dynatron in 1918. The Dynatron is

a vacuum tube electronic oscillator which uses negative resistance caused by the process of secondary electron emission. This was the first negative resistance vacuum tube oscillator. The Dynatron was also able to produce oscillations over a range of 1 Hz to 20 MHz. Originally, Hull believed that this technology would work best in radio receivers. Mentioned in papers describing the development of the Dynatron, Hull describes using magnetic control of the Dynatron by applying a magnetic field parallel to the tube axis. Hull continued to investigate and conduct experiments on the effects of magnetic fields on electrons. In an effort to develop radio receivers that do not require triode vacuum tubes, the magnetron was introduced in 1920. The Hull magnetron utilized a coaxial anode and cathode with an axial magnetic field produced by an external coil [3]. These original magnetrons are referred to as single anode magnetrons as they excluded any cavities. The single smooth bore anode showed very low efficiency and low output power. The original magnetrons were used as amplifiers and low frequency oscillators, but their potential to produce microwaves was not discovered until 20 years later by two British scientists by the names of Harry Boot and John Randall.

A split anode magnetron, by Czechoslovakian engineers August Zacek and Erick Habann emerged as the first major improvement on magnetron technology. Their design increased both the efficiency and output power. In 1940 the previously mentioned Harry Boot and John Randall would later improve on this design, which would eventually become the basis for radar development by the allies in World War II [4]. Sir Henry Tizard would lead a team of scientists researching cavity magnetron radars based off of the Boot and Randall magnetron design [5]. Although these original magnetrons were inefficient and had an unstable frequency output, they gave the allies a tremendous advantage during the war. The next great leap in magnetron technology would come in 1976 when the first relativistic magnetrons were developed. With

recent advances in pulsed power technology and cold cathode technology the magnetron could be driven at "relativistic voltages". These "relativistic voltages" enable the explosive emission mechanism from a cold cathode. Pavelesky and Befeki would introduce the A6 relativistic magnetron in 1979 [6].

1.2 Applications of High Power Microwaves

Applications for HPMs span across several areas of research and development. HPM research is being conducted in the field of directed energy weapons, high-power radar, power beaming, and plasma heating [1]. Funding over the past few decades for HPM research has been greatest for defense-driven work [1]. One advantage of HPM weapons over other directed energy weapons (DEW) is they do not have the same atmospheric propagation issues that affect lasers and charged particle beams. Defense-driven HPM work includes the Active Denial System (ADS), which is used for crowd control or riot dispersion and transmits a 94 GHz CW beam that penetrates the skin layer near the nerve endings of the target causing an intense unbearable burning sensation, and counter-electronic types of weapons such as E-bombs and CHAMP. Counter-electronic HPM weapons work by coupling electromagnetic power into the targets' electronic systems, thereby disabling them. This non-kinetic type of attack would provide little to no collateral damage compared to traditional kinetic weapons. HPM weapons would also have a deep magazine, travel at the speed-of-light, and would cost considerably less than conventional kinetic weapons.

The Counter-Electronic High-Powered Microwave Advanced Missile Project (CHAMP) is based on a cruise missile platform, built by the Air Force Research Laboratories (AFRL) Directed Energy Directorate, Kirtland Air Force Base, NM in collaboration with Boeing.

CHAMP was successfully demonstrated on October 16th, 2012 at the Utah Test and Training Range [7].

1.3 Review of Previous A6 Magnetron Experiments and Research with Axial Extraction and Transparent Cathode

A6 relativistic magnetrons with a simple mode converter and transparent cathodes have been extensively studied at the University of New Mexico. Tracking the progression of research that precedes this research, a study investigating a cathode geometry that would cause rapid-start-of oscillations in a magnetron was published in 2005 by Mikhail Fuks and Edl Schamiloglu [8]. The E_θ field within the interaction area of magnetron determines the growth time of oscillations. By creating a "transparent cathode" the E_θ field penetrates to the axis. This effect, along with the magnetic priming induced by current traveling the length of the cathode strips was simulated using the particle-in-cell (PIC) code MAGIC3D. The transparent cathode demonstrated that it indeed creates faster oscillations compared to a traditional solid cathode. In 2006, output characteristics of magnetrons using the transparent cathode [9], as well as mode conversion for axial extraction [10], were also published. In 2009 the transparent cathode was experimentally verified in a short pulse magnetron [11]. Also in 2009 a high efficiency magnetron with diffraction output (MDO) was presented by Fuks and Schamiloglu [12] and simulated in 2010 [13].

Figure 1-1: Photograph of the Magnetron with Diffraction Output (MDO).

The MDO uses a conical antenna whose cavities are continued axially along the conical horn antenna whose cross section exceeds cutoff for the radiated wave [13]. These simulations showed that the MDO can provide higher conversion efficiencies, up to ~70%, and that once again the transparent cathode provided faster start-of-oscillations compared to a solid cathode. Work was then performed on the viability, simulation, and verification of the compact MDO in 2012. This work included using novel endcap designs to suppress axial leakage currents in the compact MDO [14], verifying the Gaussian radiation pattern in an axially extracted compact MDO [15], as well as early studies on the compact MDO with permanent magnet [16].

1.4 Review of Magnetrons with Permanent Magnets at other Universities

Previous studies performed on the A6 magnetron with a permanent magnet were conducted at both the University of Electronic Science and Technology in China (UESTC) and The Technion in Haifa, Israel. At UESTC a magnet consisting of two rings constructed of

Neodymium-Iron-Boron material produced a magnetic field at the center of the magnet of 5900 G or 0.59 T.
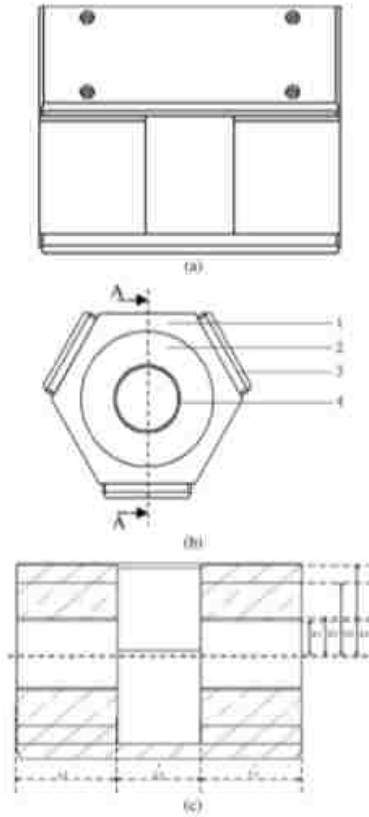
Figure 1-2: Sketch of the UESTC permanent magnet magnetron.

The uniformity of the magnetic field within the interaction area of magnetron was between 2% and 8.2%, which proved to be sufficient for operation. The A6 magnetron used in the experiment had an anode radius of 2.11 cm, vane radius of 4.11 cm, resonator angle of 20°, and an anode length of 7.2 cm. Several cathodes were used, with the "brass washer" cathode performing best. The magnetron was driven by an accelerator created at UESTC which consisted of a Marx Bank, spark-gap switch, and an oil-filled Blumlein pulse forming line. Li, Li, and Hu reported a peak output power of 540-MW with a pulse width up to 40 ns at an

operating frequency of 2.65 GHz with an efficiency of 7% with the accelerator supplying 489 kV [17].

Another magnetron design using permanent magnets was reported by A. Sayapin and A. Levin of The Technion in Haifa, Israel [18]. The study used cylindrical magnets inbuilt into hollow slots within the anode block as well as a cylindrical magnet placed coaxially inside a cold cathode producing a magnetic field within the interaction area from 0.22T-0.3 T. Both a 12- and a 6-resonator S-band magnetron with radial output were tested. The resulting microwave field produced from this geometry was not presented.

Chapter 2: Theory of Magnetron Operation and Background Physics

2. Theory of Magnetron Operation

Chapter two will introduce the basic concepts on the physics of magnetron operation, theory of operation, physics of the transparent cathode, and design parameters.

2.1 Physics of Magnetron Operation

A magnetron belongs to a class of microwave devices known as crossed-field devices. The term crossed-field is derived from the quasi-DC electric field between the cathode and the anode block of the magnetron in the radial direction being orthogonal to the axial DC magnetic field. These microwave fields can then either be extracted radially from one of the cavities in the anode or axially. Microwaves are produced from magnetrons when the drifting cloud of electrons contained in the interaction area (also referred to as an electron cloud or electron spoke) interacts with the electromagnetic fields of the slow wave structure of the anode block.

When high voltage is delivered to the cathode, explosive emission causes electrons to be emitted from the cathode into the interaction area forming a plasma around the cathode. In the absence of a magnetic field, this electron cloud would short radially to the anode block. However, after the electrons from this plasma accelerate toward the anode under the influence of the DC electric field [1], the electrons encounter the axial magnetic field, orthogonal to the radial electric field. This causes the electrons to undergo an E x B azimuthal drift about the guiding center of the magnetron. The magnetic field must be strong enough to prevent the electrons from crossing the interaction area and reaching to anode block. This relationship of electric field intensity to magnetic field intensity is what is referred to as the Hull cut-off condition and will be examined further in the next section. The relationship between magnetic field intensity, drift

velocity of the electrons in the cloud, and phase velocity of the slow wave structure of the anode

block are all critical to the production of RF in a magnetron.

The drift velocity V_d of the electron clouds within the magnetron is given by the following

expression in Equation 1.

$$V_d = \frac{ExB}{|B|^2}$$ Equation 1

where **E** is the radial electric field vector, **B** is the axial magnetic field vector and B is the

magnetic field magnitude [1]. The electromagnetic field generated by the slow wave structure of

the anode block has a phase velocity V_θ given by Equation 2:

$$V_\theta = \frac{E_r}{B_z}$$ Equation 2

where E_r is the radial electric field and B_z is the magnetic field in the azimuthal direction. In

order for the potential energy of the electrons emitted from the cathode to be transferred to the

RF field,

$$V_\theta = V_d;$$ Equation 3

that is to say, the drift velocity of the electron cloud and the phase velocity of the slow wave

structure are in resonance with each other. Resonance provides the condition for the optimal

transfer of energy. The resonant state is described by the Buneman-Hartree (B-H) synchronous

condition, which will be discussed further in the next Section.

2.2 Hull Cut-off /Buneman-Hartree Condition

As stated in the previous Section, the magnetic field intensity, electric field intensity, and the phase velocity of the slow wave structure all play critical synchronous roles in the production of microwaves. Two conditions must be met in order for oscillations to occur. The first of these is what is known as the Hull cut-off condition described in Equation 4.

$$B_c = \frac{mc}{ed_e}(\gamma^2 - 1)^{1/2} = \frac{mc}{ed_e}\left[\left(\frac{2eV}{mc^2}\right) + \left(\frac{eV}{mc^2}\right)^2\right]^{1/2}$$

Equation 4

Here, B_c is the value of the magnetic field, m is the mass of the electron, e is the electron charge, c is the speed of light, V is the voltage across the anode-cathode (A-K) gap, and d_e is the effective gap in the cylindrical geometry given by Equation 5,

$$d_e = \frac{r_a^2 - r_c^2}{2r_a}$$

Equation 5

where r_a is the radius of the anode and r_c is the radius of the cathode. If the magnitude of the axial magnetic field is too strong the electrons will travel back to the cathode. If this field is absent or too weak the electrons will travel directly to the anode. There needs to be an optimal combination of electric field and magnetic field intensities such that the electron cloud that is rotating in the cavity is confined to the cavity and the cloud barely touches the anode.

The second condition necessary for oscillations is the B-H condition, Equation 6

$$B_{BH} = \frac{mc^2 n}{|e|\omega_n r_a d_e}\left(\frac{|e|V}{mc^2} + 1 - \sqrt{1 - \left(\frac{r_a \omega_n}{cn}\right)^2}\right)$$

Equation 6

where $\omega_n = 2\pi f$ is the frequency mode of interest, and n is the mode number. The drift velocity V_d described in Equation 1 decreases with increasing magnetic field. This means that there is a maximum axial magnetic field above which the electrons are too slow to be resonant.

The Hull cut-off and B-H conditions work together to define a specific area of operation involving intensities of the radial electric field and the axial magnetic field. To briefly summarize, the magnetic field intensity must be sufficiently intense to prevent electrons from reaching the anode block, but not so intense that it slows down the electrons to the point where the drift velocity is too slow for resonance. Figure 2-1 [1] is a graphical representation of the B-H condition, the Hull cut-off condition, and the magnetic field range for oscillation.
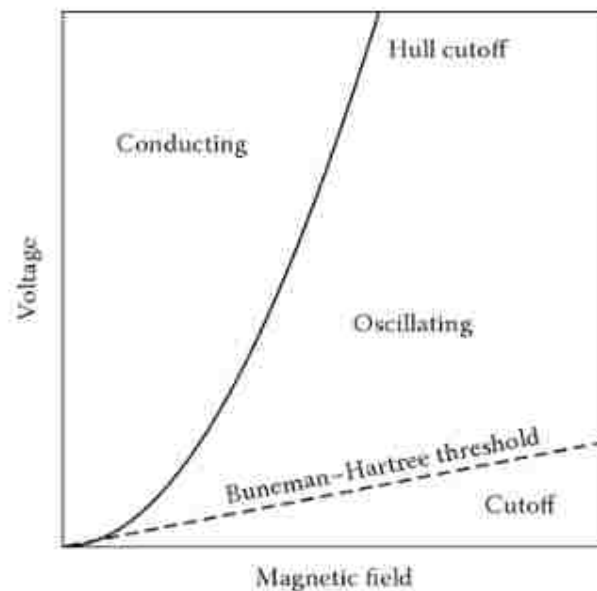
Figure 2-1: Graphical representation of the Buneman-Hartree/Hull cut-off conditions.

2.3 Formation of Spokes, Modes of Operation, and Design Parameters of Magnetrons

The 6-vane, 6-cavity geometry of the anode block in an A6 magnetron constitutes the slow wave structure that gives rise to the RF fields in the interaction area. As electrons are emitted in the interaction area and the RF fields reach sufficient intensity to interact with the electron cloud,

11

which is already under the influence of the DC electric field and the magnetic field, the electrons will begin to bunch together according to the phase variations of the slow wave structure, and form spokes. The RF fields grow with intensity according to the input voltage applied to the magnetron. There are a variety of possible operating modes that can be developed within the slow wave structure. Magnetron modes are designated by mode number n, where n is the number of times the microwave field pattern repeats itself in one revolution around the anode [1]. The angular spacing between N cavities is defined as

$$\Delta\theta = \frac{2\pi}{N}.$$ Equation 7

The phase shift between adjacent cavity resonators for the nth mode is

$$\Delta\theta = \frac{2\pi n}{N}.$$ Equation 8

Two common operating modes in magnetrons are the π-mode and 2π-mode. In the π-mode, the phase of the RF fields is reversed from one cavity to the next. In the 2π-mode, the fields are consistent in every cavity throughout the anode. The electric fields for the π-mode and 2π-mode can be seen in Figure 2-2 [1].
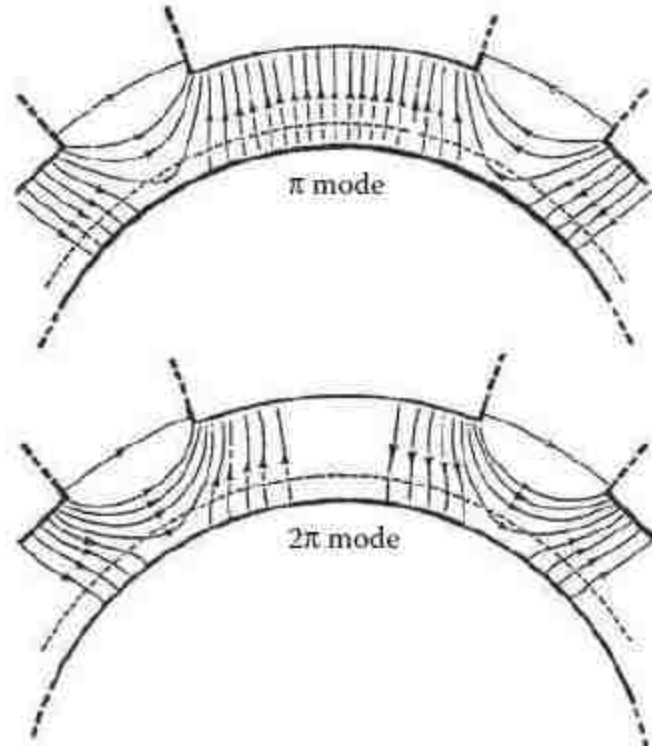
Figure 2-2: Diagram illustrating the π-mode and 2π-mode.

The electron cloud will form spokes when the electrons interact with the RF fields of the anode according to the operating mode. When an electron in rotation around the interaction area is in phase with the RF field, it will be drawn closer to the anode. When an electron is out of phase with the RF field it will drift back towards the cathode. Thus, a magnetron operating in π-mode, in which the electric field is reversed from one cavity to the next, will have three spokes. In the 2π-mode, the electron cloud will form 6 spokes. The formation of these spokes, as well as the competition between modes, is also dependent on the cavity fill time, as described by Bosman et al. [9]. The relationship between cavity fill time and voltage rise time and their effects on mode competition will be described further in Section 3.6.

Popular competing modes within the A6 magnetron are the $4\pi/3$-mode and the $2\pi/3$-mode. The dispersion relation relates the frequency for a given mode ω_n, to the mode number n. The dispersion relation of the A6 magnetron is given by Equation 9

$$f_n = \frac{(\omega_n \Delta\theta)}{2\pi}$$ Equation 9

and can be viewed in Figure 2-3.
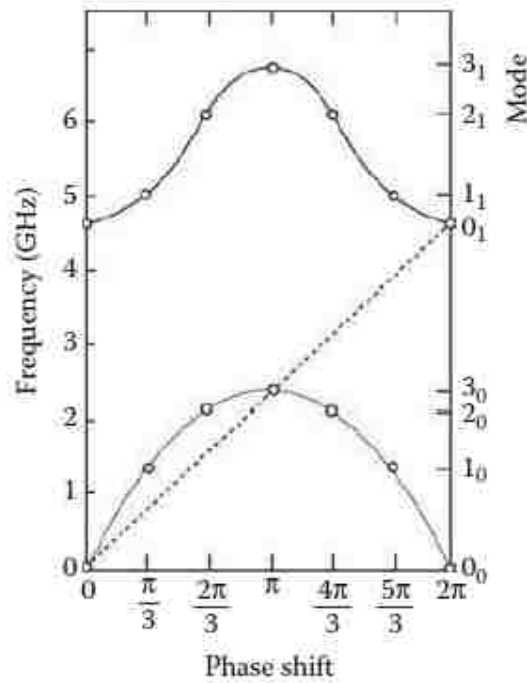
Figure 2-3: Dispersion relation corresponding to the A6 magnetron.

Additionally, the dispersion relation for the A6 magnetron was simulated and analyzed using Poisson Superfish, a program created at Los Alamos National Laboratory, which calculates magnetic and electric fields of 2D geometries [19]. The calculated dispersion relation is shown in Figure 2-4.

14
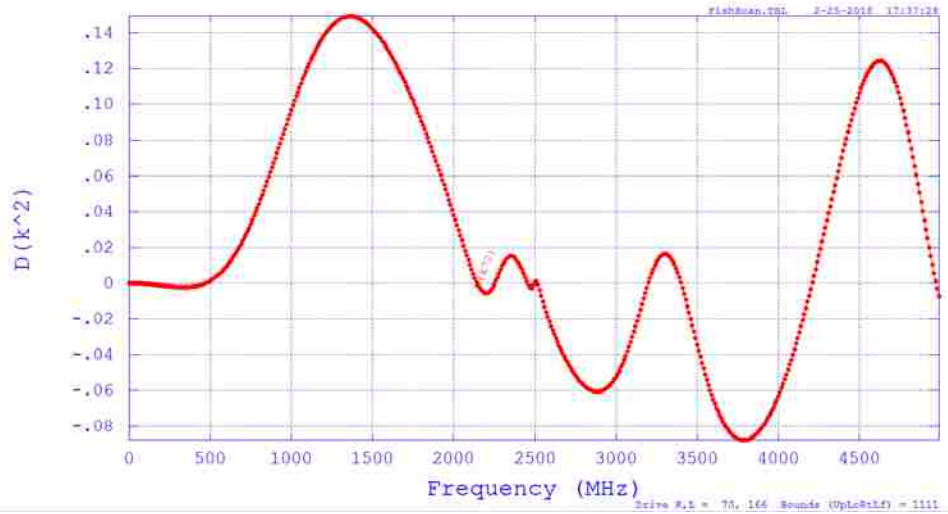
Figure 2-4: Dispersion relation of the A6 magnetron with a transparent cathode calculated using Poisson Superfish.

The frequency of these modes is given by Equation 10

$$f_\pi = \frac{\omega_\pi}{2\pi} = \frac{c}{\lambda} = \frac{c}{4L_a}$$

Equation 10

where $L_a = r_v - r_a$.
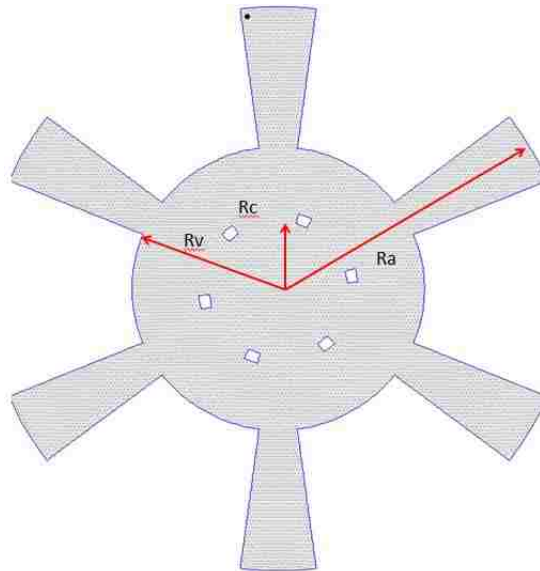
Figure 2-5: Diagram of the A6 magnetron with a transparent cathode.

According to Collins [20]**,** L_a is approximately $\lambda/4$, where λ is the free space wavelength of the desired frequency of output radiation. The resonator length, *h,* will also determine the operation mode of the anode block according to Equation 11.

$$\left(f_n^g\right)^2 = (f_n^0)^2 + \left(\frac{gc}{4h}\right)^2 , g = 1,2,3, ...$$

Equation 11

Mode competition will be prevalent in anodes when $h > \lambda$. Typically r_c will range between one-eighth and one-fifth of a wavelength, and r_a will range from one-sixth to one-third of a wavelength. The dimensions of the A6 magnetron that is the focus of study presented in this thesis are as follows: the length of the resonator *h*=7.2 cm, the radius of the anode $r_a = 2.11$ cm, the anode block resonator $r_v = 4.11$ cm, and the radius of the cathode $r_c = 1.58$ cm.

2.4 Mode Converter

In order for the RF fields to be extracted axially into a TE_{11} mode from the end of the anode as opposed to radially from one of the cavities, a simple mode converter must be used. The mode converter used in this study electrically opens two diametrically opposite cavities and covers the others with a metal plate. The TE_{11} mode in a cylindrical waveguide produces a Gaussian profile of the electric field. The Gaussian distribution of the TE_{11} mode is especially useful for DE weapons, as the maximum electric field of the pulse is found on-axis. This allows for maximum power on target for DE weapons as mentioned in Chapter 1 [1]**.** The field distribution of the TE_{11} mode in a cylindrical waveguide, as well as the Gaussian distribution of electric field for the TE_{11} mode, are shown in Figure 2-6**.**
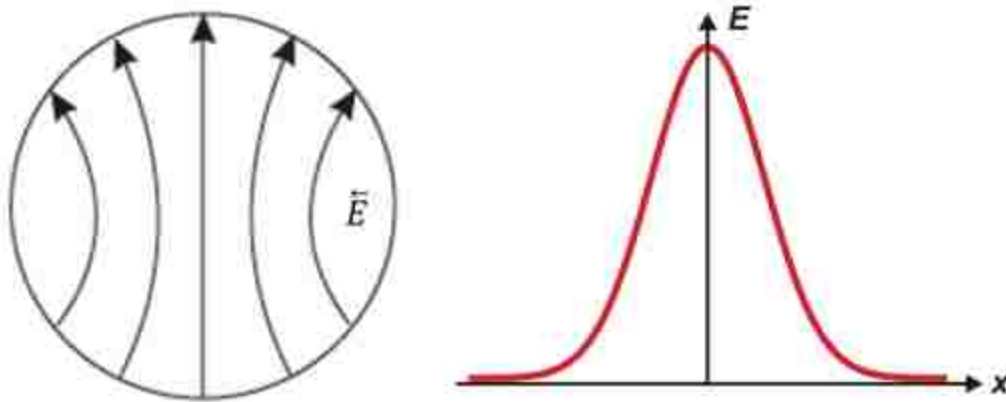
Figure 2-6: Field distribution of the TE11 mode (left) and Gaussian distribution of electric field for the TE11 mode (right).

As mentioned in Section 1.3, Mikhail Fuks, Nikolay Kovalev, Andrey Andreev, and Edl Schamiloglu researched and presented various methods for mode conversion in a magnetron with axial extraction [10]. Their work was accomplished using the MDO. Magnetrons primarily operate in π or 2π mode as they are nondegenerate; all other modes are azimuthally degenerate. Ordinarily in a 6-cavity magnetron operating in π-mode, where the phases of the electric field vary by 180° from cavity to cavity, the mode radiated axially into the conical horn antenna corresponds to the TE_{31} mode.
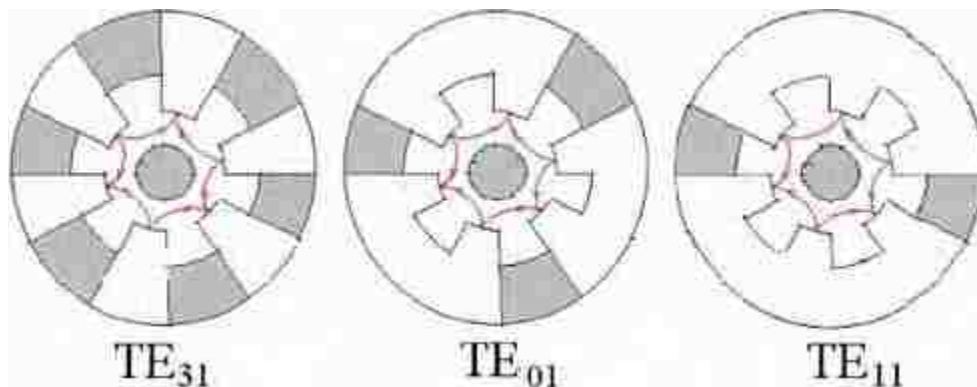
Figure 2-7: Examples of simple mode converters and corresponding modes in an MDO.

17

When every other cavity of the magnetron becomes electrically open, the antenna is excited by electric fields with identical faces, which correspond to the TE_{01} mode. In the case where only two diametrically opposed cavities are electrically closed, the cylindrical horn antenna will then radiate the lowest mode, TE_{11}. From the TE_{11} mode, a Gaussian radiation pattern can be produced. Figure 2-8 shows the mode converter used with a transparent cathode and a permanent magnet. The mode converter is comprised of two metal plates that screw directly onto the anode vanes of the compact MDO. The simple mode converter does not alter or interfere with the existing geometry of the magnetron or the cylindrical horn antenna.
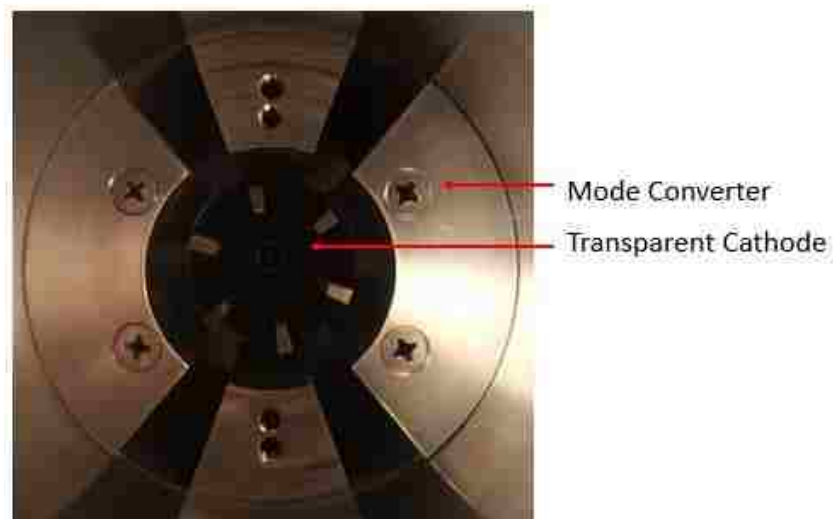
Figure 2-8: Mode converter that electrically opens two opposing cavities and is driven by a transparent cathode.

2.5 Physics of the Transparent Cathode

The transparent cathode was initially created to increase the rate-of-oscillations in magnetrons by increasing the synchronous electric field and providing magnetic priming due to the magnetic field generated by the loss current from the longitudinal strips of the cathode [8]. Traditionally, conventional magnetrons use a solid cathode with azimuthally uniform electron

emission. The RF fields in these conventional magnetrons have a rather slow start and slow rate of build-up of oscillations, which makes them unattractive for short – pulse operation [11]. The transparent cathode is comprised of a hollow cathode with longitudinal strips that act as individual emitters, shown in Figure 2-9.
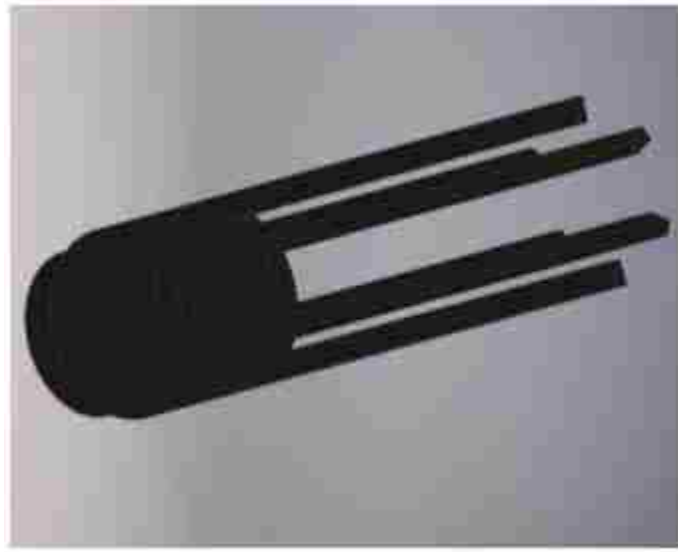
Figure 2-9: Isometric view of a 6-emitter transparent cathode.

By removing the strips and not having a solid cathode, the resulting cathode was then "transparent" to the azimuthal RF electric field. Two mechanisms contribute to a faster-start-of oscillations, cathode priming and magnetic priming. The technique of cathode priming was invented at the University of Michigan (UM) [21]. At UM, periodic emitting zones of electrons along the solid cathode force electrons to bunch into the desired mode. The transparent cathode used in this study, which was discovered independent of UM's cathode priming, follows the same premise as each of the 6 emitting strips force the electrons to bunch into the desired mode. The second mechanism, also pioneered at UM [22], is magnetic priming. Whereas at UM magnetic priming was attributed to permanent magnets employed around the perimeter of the magnetron, magnetic priming occurs self-consistently in the transparent cathode when the axial

currents along the cathode strips produce individual magnetic fields along the strips, as expressed by Ampere's Law, Figure 2-10.
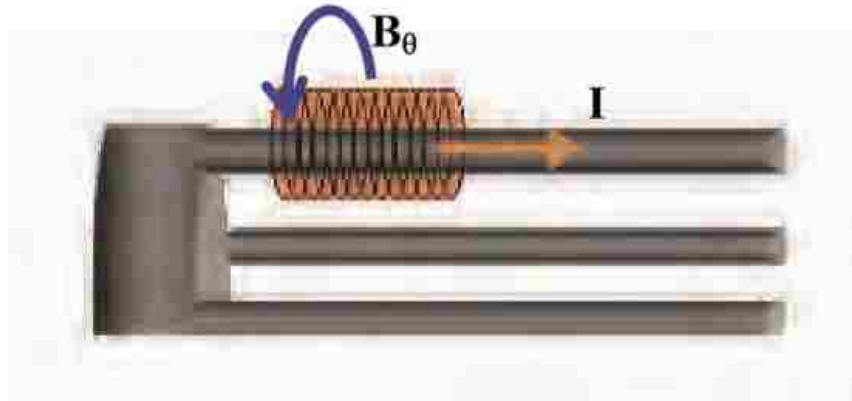
Figure 2-10: Magnetic field B_θ produced from axial currents through each emitter.

The magnetic fields produced by the magnetic strips introduce an azimuthal perturbation in the axial magnetic field. The transparent cathode has demonstrated [11] higher radiation power, higher electron efficiency, and stable microwave generation compared to performance of the solid cathode. Mode competition can be suppressed with proper azimuthal orientation of the transparent cathode and the appropriate selection of magnetic field.

Chapter 3: Simulations of a Compact MDO with Permanent Magnet

3. Simulations of the Compact A6 Magnetron with a Permanent Magnet

Prior to the installation and testing of the permanent magnet on the compact MDO, several simulations were performed to identify the ideal operating parameters that would produce the highest RF output.

3.1 Overview of MAGIC

MAGIC3D is an electromagnetic particle-in-cell finite-difference, time-domain (EM PIC FDTD) software used for solving plasma physics processes. It has been used at UNM as well as several other institutions to aid in the modeling and development of plasma physics-based devices. Currently it is being used at UNM to model and optimize an A6 compact MDO with a permanent magnet, as well as various other novel slow wave structures, backward wave oscillators, and cathode designs. The code simulates the electrons and plasma from an initial state and simulates how they interact as the processes evolve in space and time [23]. MAGIC uses Maxwell's time-dependent equations to obtain values for electromagnetic fields, and uses the Lorentz force equation to solve relativistic particle trajectories. The plasma and fields are solved within a determined geometry that represents the device one wishes to simulate. MAGIC3D also allows for spatially variable gridding in order to specify finer grids in areas that require greater resolution. MAGIC3D gives tremendous flexibility to the user when determining ideal operating conditions, i.e. input voltage magnitude, input voltage pulse rise time, and magnetic field intensity. It also gives the user the flexibility to manipulate physical dimensions of certain components and compare the outputs of such manipulations. Physically creating

various components of different dimensions and then experimentally testing them would be cumbersome, costly, and outright impractical.

3.2 Simulation Set-up

The geometrical set-up for the simulations is shown in Figure 3-1. All geometries in the simulation were created within in a cylindrical coordinate system. The geometry was chosen to be defined in the cylindrical coordinate system to accommodate the cylindrical compact MDO.
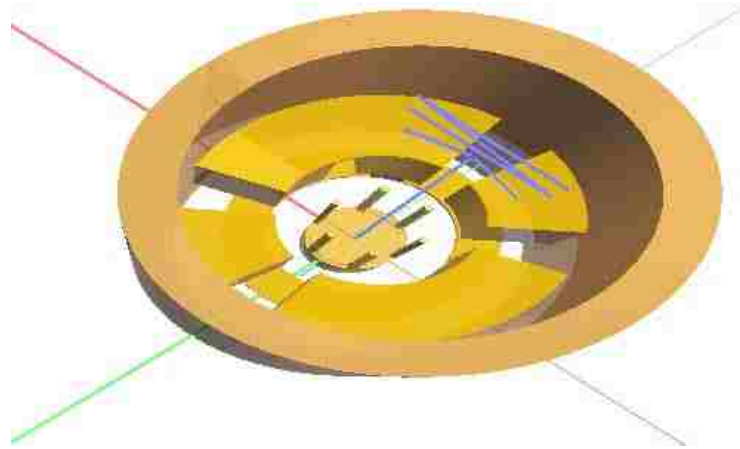
Figure 3-1: 3D view of the A6 compact MDO used in simulations.

The compact MDO in this study consists of a 6-vane anode block, a 6-emitter transparent cathode, a diametrically opposed mode converter, and a strap. The 6 cavities of the A6 magnetron have an angular width of 20°, an axial length of 7.2 cm, and a radius of 4.11 cm. The radius of the vanes is 2.11 cm, which corresponds to the radius of the interaction area. The transparent cathode has 6 emitters of length 7.2 cm and an angular width of 10°. The mode converter is located on the upstream end of the magnetron and electrically closes two diametrically opposed cavities. The strap is attached to the upstream end of the anode block and is shown in Figure 3-2.
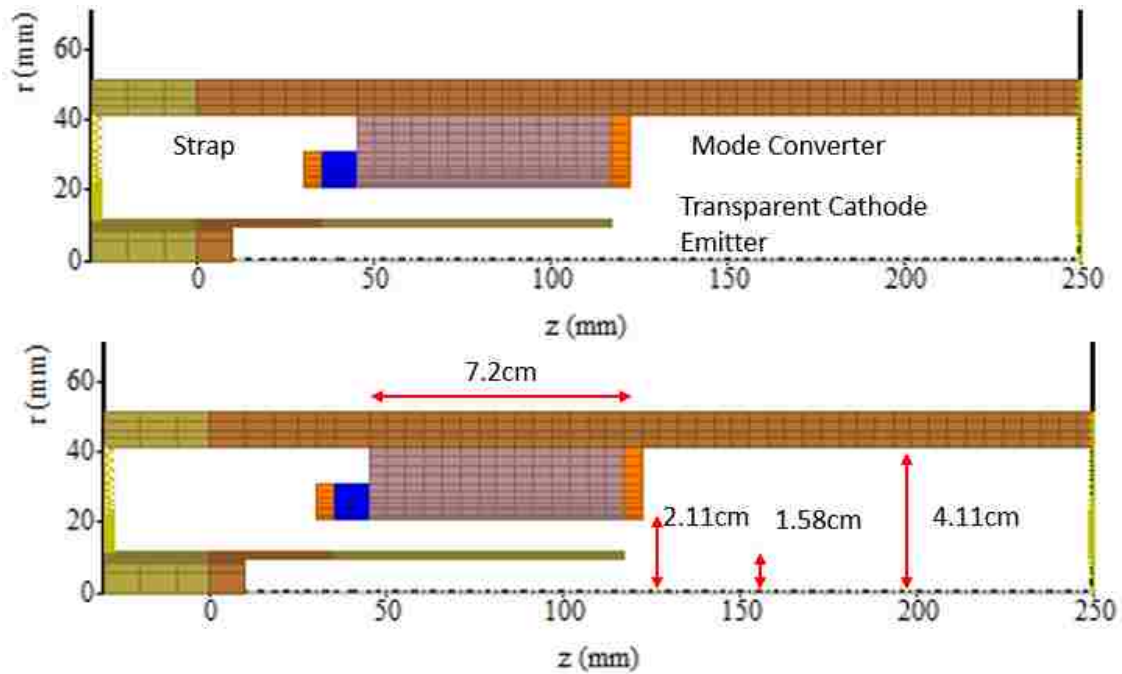
Figure 3-2: 2D cross section of compact MDO used in simulations plus relevant dimensions.

In order to assess the performance of the compact MDO at different input parameters, several

diagnostics were added to the simulations. The anode current is measured along the length of the

vane in the interaction area. The leakage current diagnostic is measured at in intermediate point

between the interaction area and the output port and provides information regarding the amount

of input current that is not being converted to RF and escaping the cavity along magnetic field

lines. The power output is measured on the output port of the simulation set-up. Finally, a Fast

Fourier Transform (FFT) is applied to the output electric field. The FFT is the most important

diagnostic in assessing the performance of the compact MDO. As explained in previous

Chapters, the frequency of the power output for the compact MDO is determined according to

the mode radiated axially out of the compact MDO. For the geometrical size of the anode block,

transparent cathode, and the effect of the mode converter on the downstream end of the anode

block, the π-mode frequency corresponds to 2.5 GHz.

3.3 Permanent Magnet

The permanent magnetic field is specified in MAGIC by use of the "preset" function to initialize the field. This is accomplished by first defining functions to represent the volume of the interaction area in both the axial and radial directions, as well as the intensity of the magnetic field and then using the B3ST and B1ST arguments to make create magnetostatic fields for both the axial and radial directions. These fields are never changed throughout the entirety of the simulations.

3.4 Test Matrix

The following test matrix was simulated in order to find the ideal operation parameters that would produce the highest extracted RF field. Since the magnetic field is produced by a permanent magnet and is, therefore, fixed, an increasing array of input voltages were tested in order to find the appropriate input voltages that would correspond to the B-H and Hull cut-off conditions, as mentioned in 2.2. Also, a combination of voltage rise times and pulse lengths were tested. Mode competition between the nondegenerate π-mode and degenerate $4\pi/3$-mode is strongly correlated to cavity fill time, as described by Bosman [9]. Cavity fill time and its effects on mode competition in the A6 magnetron will be further discussed in Section 3.5. Input voltages range from 285 kV to 350 kV and at each voltage a pulse length of both 30 ns and 100 ns were tested. At each pulse length, voltage rise times of 4 ns, 8 ns, and 16 ns were tested. The final test matrix consists of a total of 84 simulations. The results from the test matrix can be found in appendix A.

3.5 Results

The results from the test matrix above indicated that the ideal operational parameters for the permanent magnet compact MDO are an input voltage range between 300-310 kV at a pulse

24

width of 30 ns with a voltage rise time of 4 ns. Although similar extracted RF powers were

simulated towards the higher end of the voltage scan, it is reasonable to consider the voltages

between 300-310 kV to be more efficient, as the same RF output was recorded with less input

voltage. From the results in Appendix A, it can be seen that there is significant mode

competition for every simulation with a voltage rise time greater than 4 ns. Mode competition

from the $4\pi/3$-mode correlates to an output frequency of 2.73 GHz and has significantly lower

power output than the π-mode, which has an operating frequency of 2.5 GHz. Also, it can be

seen from the results of the test matrix that the π-mode output cannot be sustained throughout the

duration of a 100 ns pulse, even for the ideal range of 300-310 kV input voltage with a rise time

of 4 ns; the π-mode degenerates into the $4\pi/3$-mode. Figure 3-3 shows the FFT of input voltages

form 285 kV to 295 kV, and the corresponding dominant spoke pattern of each input voltage

displaying the input voltage threshold for π-mode oscillations.
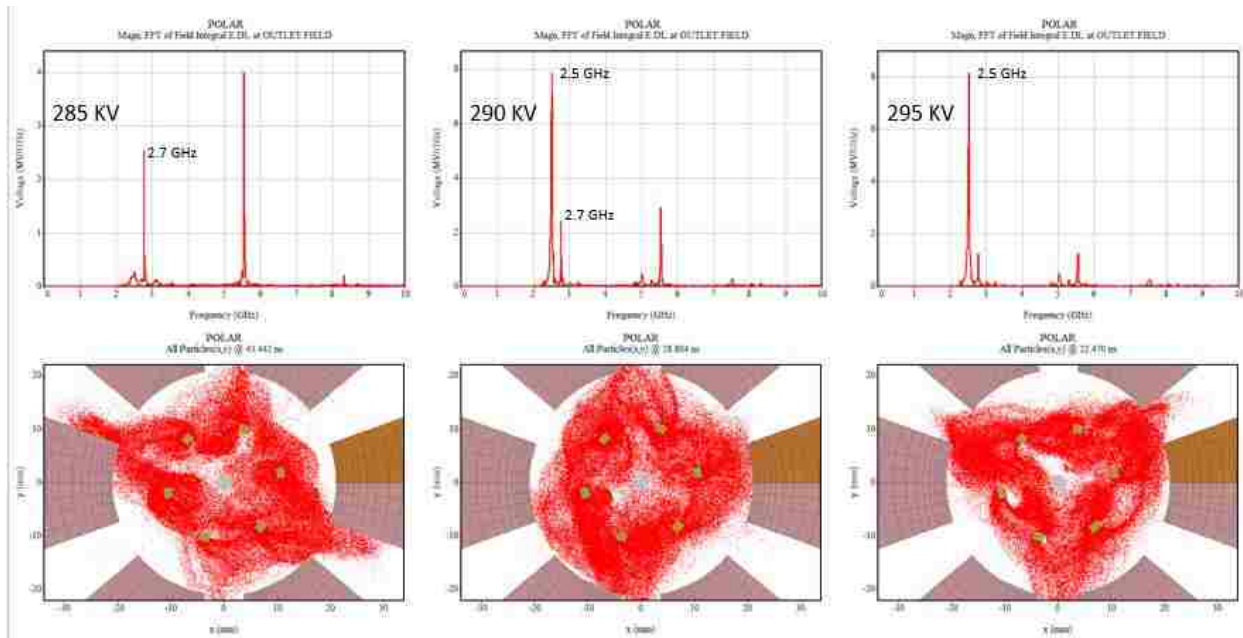
Figure 3-3: Dominant spoke patterns and FFT of resulting microwave below threshold and at threshold from MAGIC simulations.

3.6 Cavity Fill Time and Mode Competition

One potential drawback of using a transparent cathode is the higher probability of mode competition with the pulses with long voltage rise times [9]. The transparent cathode, as mentioned in Section 2.5, promotes the growth of all resonant modes because of the cathode priming process. In the study it was demonstrated that "the self-excitation of oscillations in resonant microwave sources strongly depends on the relation between the cavity fill time and the voltage rise time, or, more correctly, on the time of increasing azimuthal electron drift velocity as the voltage grows." From the simulation results presented in Appendix A, we can see that the π-mode frequency of 2.5 GHz was more frequently radiated in the simulations with a voltage rise time of 4 ns. Voltage rise times of 8 ns and 16 ns generated the $4\pi/3$-mode of 2.73 GHz. For slow turn-on, meaning that the cavity fill time is less than the voltage rise time, there is sufficient time for the modes with lower phase velocity, i.e. the $4\pi/3$-mode, to develop once their B-H thresholds, mentioned in Section 2.2, are exceeded. The transparent cathode may still be a suitable candidate in magnetrons with long voltage rise times if the electron emission process were somehow controlled so that the electrons would only be emitted when the electric field reached a satisfactory level that would favor the operating mode [24]. Figure 3-4 is an example of a 100 ns pulse width, 300 kV input in which mode competition between the π-mode and $4\pi/3$ modes is evident. The drop off of power around the ~50 ns mark is attributed to the less efficient $4\pi/3$ mode emerging as the dominant resonating mode.
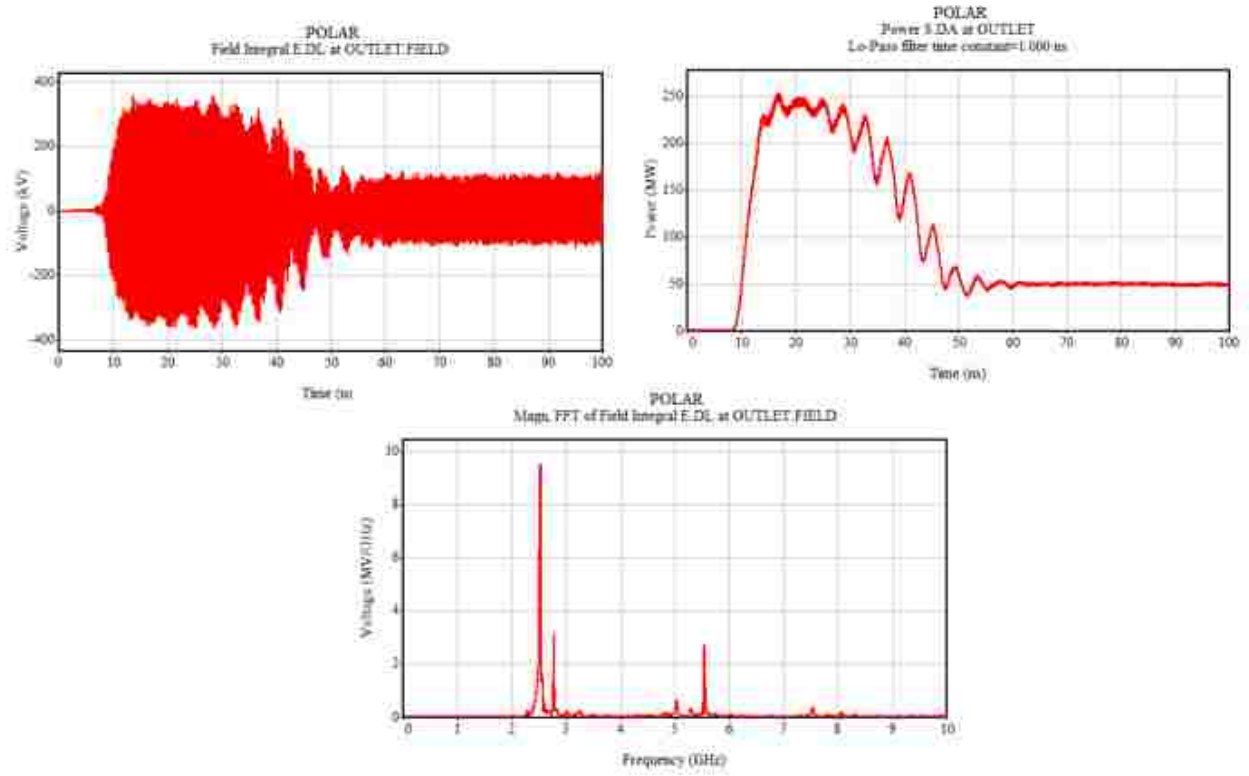
Figure 3-4: 100 ns pulse width resulting in mode competition and loss of output power.

Chapter 4: Experimental Set-up

4.   Experimental Set-up

The experimental set-up for the verification of the simulation results of the permanent magnet A6 compact MDO is presented in this Chapter. Assembly of the compact MDO with permanent magnet, the PULSERAD accelerator used to drive the magnetron, and all diagnostics used in the verification of the simulation results will be discussed as well.

4.1 PULSERAD Pulser

The pulsed power high voltage source used in this permanent magnet compact MDO study is the PULSERAD-110a manufactured by Physics International Corporation. The modified PULSERAD-110a consists of a 6-stage Marx bank that charges a 20 Ω, 30 ns coaxial pulse forming line (PFL), a self-breaking oil switch that discharges into a matched 20 Ω coaxial transmission line, an oil-vacuum interface, and a vacuum chamber. The load, the A6 compact MDO with permanent magnet in this case, is assembled directly onto the vacuum chamber. The PULSERAD-110a is capable of delivering 6.3 GW to the matched load. The modified PULSERAD accelerator is capable of producing a voltage pulse of 350 kV with a voltage rise time of less than 4 ns and a pulse duration of 30 ns. The following Sections will discuss the components of the accelerator.

4.2 Marx

The 6-stage Marx bank, shown in Figure 4-1, consists of 6 bipolar, 0.050 µF case-center-grounded capacitors, charged in parallel to ~± 20-35kV and discharged in series through 7 SF_6 gas switches.
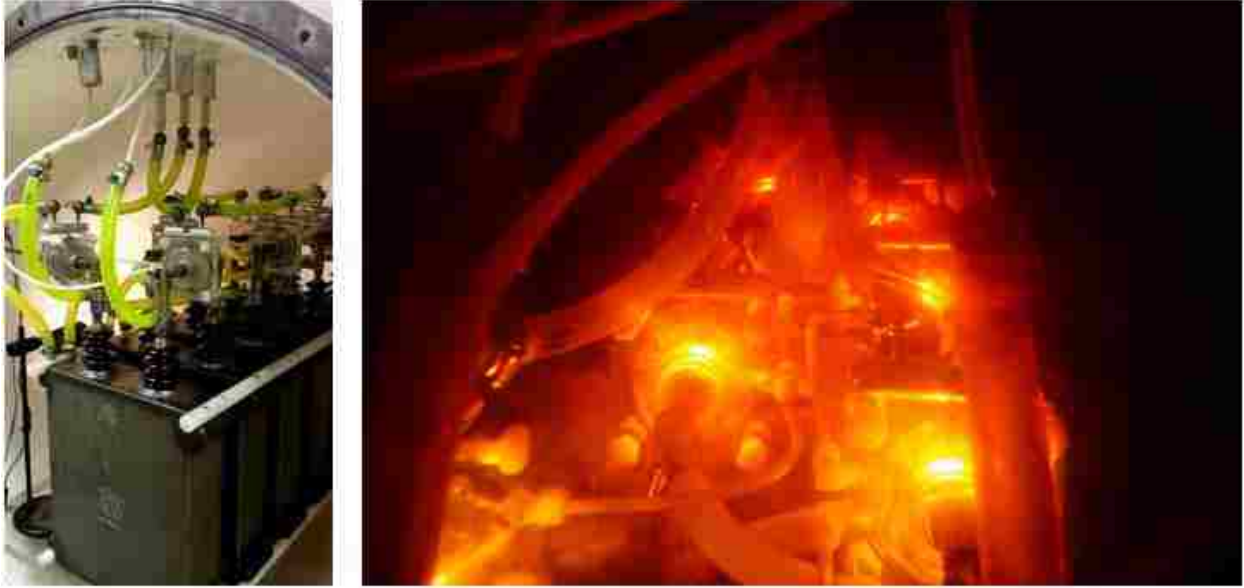
Figure 4-1: Photograph of the PULSERAD Marx bank (left) and switches closing during operation (right).

The first three switches in the series of 7 are externally triggered using a 50 kV pulse delivered by an external krytron trigger circuit. An image taken from a long exposure camera shows the switches breaking down in series. After the first three switches are triggered, the potential across the remaining switches becomes sufficiently high to close the remaining switches in series. The voltage output of the Marx connects directly into a 7 Ω CuSO₄ (copper sulfate) resistor and to the 20 Ω coaxial PFL. The PULSERAD accelerator provides a ringing gain of 1.74 by making the Marx bank capacitance greater than the PFL capacitance. Because of this ringing gain the voltage delivered to the 20 Ω pulse forming line is multiplied by a factor of 1.74 as described Equation 12.

$$V_{pfl} = V_{marx}\left(\frac{C_m}{C_m + C_{pfl}}\right)(1 - \cos \omega t).$$

Equation 12

In Equation 12, V_{pfl} is the voltage on the pulse forming line, V_{Marx} is the discharge voltage of the Marx bank, $C_m = 8.33$ nF is the equivalent series capacitance of the Marx bank, and $C_{pfl} = 1.2$ nF

is the capacitance of the coaxial pulse forming line. When the cosine term is equal to -1 and the

ratio of C_m to C_{pfl} is equal to 0.871 a maximum gain factor of 1.74 is obtained [25] [26]. The

V_{Marx} term in the equation is determined by the oil gap switch described in the next Section.

4.3 Oil Spark Gap Switch

As mentioned in the previous Section, the voltage discharged from the Marx is determined

by the self-breaking oil gap switch. The distance between conductors of the oil gap switch,

shown in Figure 4-2, can be manually adjusted to adjust the voltage discharge of the Marx.
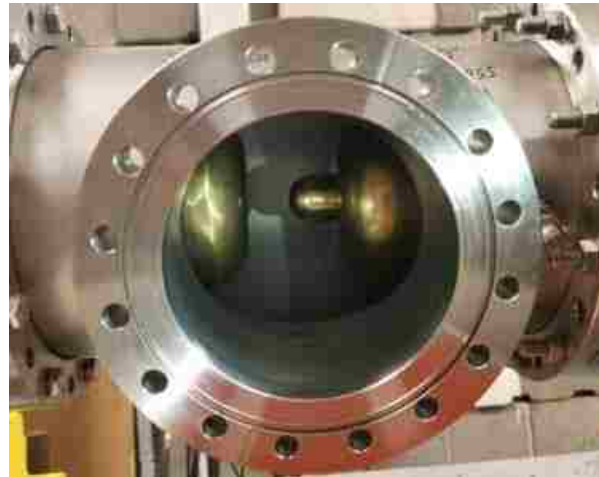
Figure 4-2: Photograph of the oil gap switch.

As described in Section 3.6, mode completion can arise when the cavity fill time (about

7-8 ns) is less than the voltage rise time. This means that controlling the voltage rise time is

critical for efficient magnetron performance. The oil gap switch is a low-inductance peaking

switch. Limiting the inductance subsequently limits the rise time of the voltage pulse by

allowing only a single breakdown path between electrodes. The oil gap switch is immersed in

high voltage dielectric oil that has a dielectric constant ε_r of 2.1. Equation 13-Equation 16

determine the rise time of the oil gap switch:

$$\tau_t = (\tau_R^2 + \tau_L^2)^{1/2} \qquad\qquad\qquad \text{Equation 13}$$

$$\tau_R = \frac{5}{(NZE^4)^{1/3}} \qquad\qquad\qquad \text{Equation 14}$$

$$\tau_L = \frac{L}{NZ} \qquad\qquad\qquad \text{Equation 15}$$

$$L = 2d \ln\left(\frac{b}{a}\right), \qquad\qquad\qquad \text{Equation 16}$$

where τ_t is the total rise time, τ_R is the time constant for the resistive phase of the switch, τ_L is the time constant for the inductive contributions to the rise time, N is the number of channels (1), Z is the impedance of the driving circuit (40 Ω), E is the mean electric field (980 kV/cm), L is the inductance per switch channel, d is the switch gap (roughly 0.61cm), a is the radius of the channel (0.01cm), and b is the radius of the disc feeding the channel (0.005cm). The 10-90% rise time is therefore calculated to be τ_t=3.5ns [24].

The distance between electrodes can be manually adjusted by rotating the extruding center of the inner conductor. As the PFL electrode rotates, the extruding center moves in or out at a rate of 14 threads per inch, which translates to 1.814 mm/turn [25]. For experiments with the compact MDO and permanent magnet the gap between the two electrodes was maintained at 5.2 mm. A photograph taken of the oil gap switch during breakdown can be seen in Figure 4-3.

Figure 4-3: Photograph of the oil gap switch pre-fire (left) and during operation (right).

4.4 Permanent Magnet

The permanent magnet used in this experiment is a Neodymium Iron Boron (NeFeB) Grade N40M rare earth magnet manufactured by Electron Energy Corporation located in Landisville, PA. The outer diameter of the entire magnet is 9.5 inches with an inside diameter 3.543 +/- 0.005 inches. The length of the magnet is 7.5 inches. The magnet as a whole is constructed of 8 identical magnets which are then assembled into it's final cylindrical form. The assembled magnet has a total mass of 50 kg. A photograph of the magnet prior to the installation of the phenolic housing is shown in Figure 4-4.

Figure 4-4: Photograph of the NdFeB permanent magnet as-delivered at UNM.

The grade N40M magnet has the following magnetic properties:

- B_r = 1.26 T minimum to 1.29 T maximum

- H_c = 11.26 kOe minimum

- iHC = 14kOe minimum

where B_r is the residual induction, H_c is the coercivity, and iHc is the intrinsic coercivity. Figure 4-5 shows the magnetization direction in both the bore of the magnet and the magnetic material itself.
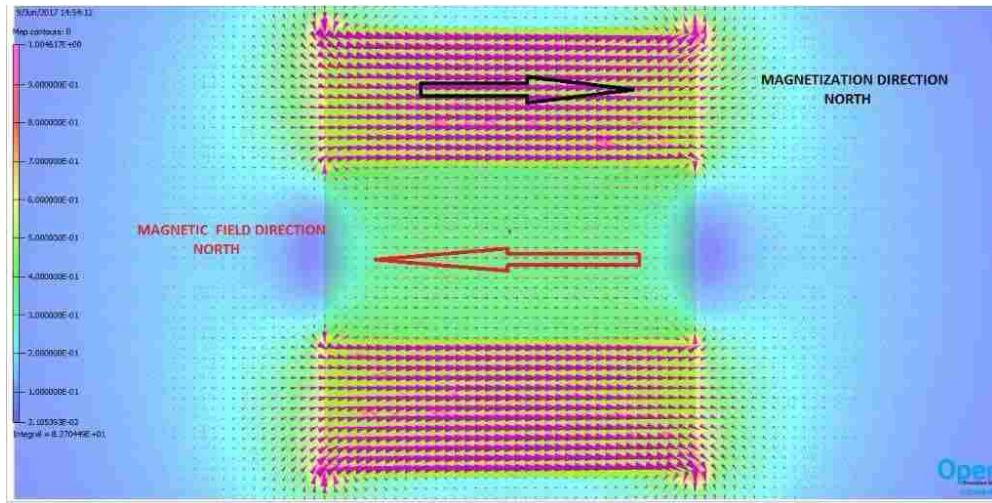
Figure 4-5: Magnetization direction within bore of magnet and in the magnetic material.

The length of the magnet was chosen so that the magnetic field in the bore of the permanent magnet fully maintains ~96% uniformity throughout the length of the magnetron vanes, which corresponds to the interaction area. Before handling the magnet to assemble onto the compact MDO a phenolic housing was place on the magnet. This housing was designed and constructed as a safety precaution in the event that stray metallic material is drawn to and impacts the magnet. A photograph of the magnet with the assembled phenolic housing is shown in Figure 4-6**.**

Figure 4-6: Photograph of the permanent magnet installed in a phenolic housing.

4.5 Compact MDO and Permanent Magnet Assembly

The compact MDO was assembled onto the PULSERAD accelerator prior to the installation of the magnet. Following the self-breaking oil gap switch, the coaxial transmission line is filled with oil between the inner and outer conductors. An oil vacuum interface is then attached to the end of the coaxial line and connects the vacuum chamber to the oil filled line. The inner conductor of the transmission line is continued through the oil vacuum interface and into the vacuum chamber by the use of the cathode shank. The cathode shank holds the transparent cathode in place in the center of the interaction area of the magnetron cavity. The first Rogowski coil is then attached to the end of the vacuum chamber. This Rogowski coil is the current diagnostic used in measuring the input current entering the magnetron. The compact MDO is then attached directly onto the Rogowski coil. The transparent cathode is then very carefully attached to the cathode shank and concentricity with the compact MDO was ensured. Next, the permanent magnet with the phenolic housing is slid over the compact MDO. Prior to assembling the permanent magnet onto the compact MDO in its final configuration, a procedure for safely handling and moving the magnet was developed and practiced.
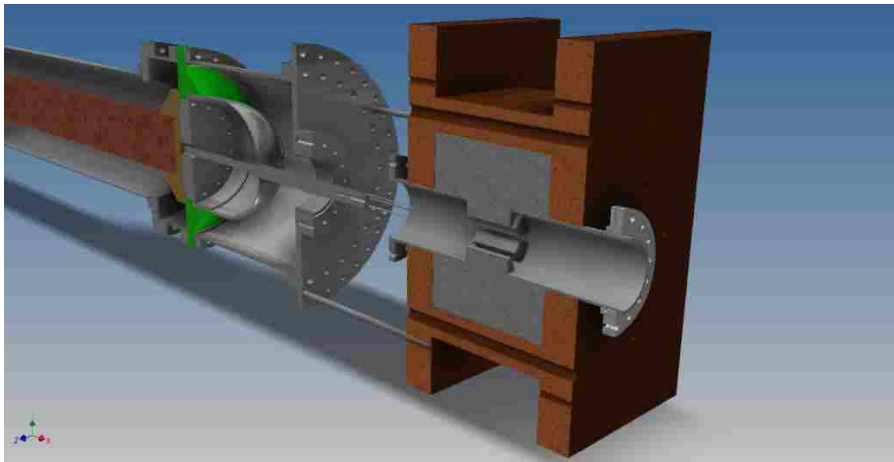
Figure 4-7: Assembly drawing of the permanent magnet and compact MDO onto PULSERAD accelerator.

The size and intensity of the permanent magnet make safe handling of the magnet of paramount importance. Once the permanent magnet is in final position, the second Rogowski coil is attached to the downstream end of the compact MDO. This is the diagnostic for measuring leakage current. An 8" beam dump is then attached to the end of the compact MDO and second Rogowski coil. The beam dump is used to collect leakage current and prevent it from reaching and damaging the dielectric window at the end of the conical horn antenna, which is attached to the end of the beam dump. Lead bricks were then placed around the phenolic housing (and consequently the anode block) to shield X-rays that are emitted when the high energy electrons bombard the anode block and beam dump. Figure 4-8 shows the fully assembled permanent magnet on the compact MDO attached to the PULSERAD accelerator.

Figure 4-8: Photograph of the final assembly of the permanent magnet onto the PULSERAD accelerator.

The oil gap switch was then adjusted to a distance of 5.2 mm in order to provide the necessary condition for operation at 300 kV-350 kV. D-dot voltage probes were attached to the outer conductor of the coaxial transmission line as mentioned previously to measure PFL voltage and load voltage. The D-band waveguide was place at a distance of 70 cm in front of the horn antenna.

4.6 Conical Horn Antenna

The simplest and most widely used microwave antenna is the horn antenna [27]. The horn antenna, as mentioned in the previous Section, is attached to the end of the beam dump connected to the compact MDO. The antenna is needed to radiate the fields of the microwave with minimal reflections and increase the directivity and gain of the emitted radiation pattern. Work has been done previously to ensure that the antenna can handle the high-power output of the compact MDO and it was shown experimentally that the horn is sufficient to radiate 500 MW [26].

4.7 Diagnostics

Two Rogowski coils, two D-dot probes, and RF diagnostics were used to characterize the performance of the compact MDO and will be discussed in detail in the following Sections. All diagnostics are cabled into the screen room and captured on oscilloscopes for analysis.

4.8 Current Diagnostics

Two Rogowski coils were used to measure both the input current to the magnetron as well as the leakage current at the output of the magnetron. Knowing both the input current and leakage current are important diagnostics when determining the operation efficiency of the magnetron. A Rogowski coil consists of tightly wound wire wrapped around a non-magnetic core.

Both Rogowski coils used on either end of the magnetron are identical. The coils are placed in line with the magnetron and measure the amount of current passing through the center of the coil. Figure 4-9 is a graphical representation of the Rogowski coil operation. These coils are designed to measure currents of magnitudes in the 10s-100s kA.
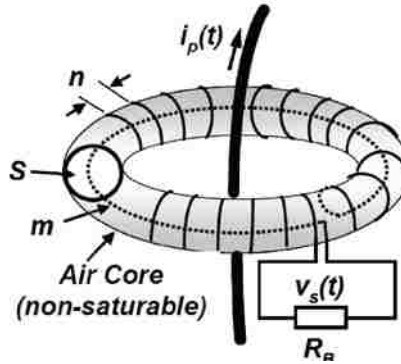
Figure 4-9: Graphical representation of Rogowski coil operation.

- Mutual coupling between primary and secondary windings is weak. In order to obtain high quality measurements, Rogowski coils should be designed to meet the following specifications: The relative position of the primary conductor inside the coil loop should not affect the coil output signal, and the impact of nearby conductors that carry high currents on the coils output signal should be minimal.

- Mutual inductance M, Equation 17, must have a constant value for any position of the primary conductor inside the coil loop. In Equation 17, n is the number of turns of the wire wound around the non-magnetic core, and S is the cross-sectional area of the coil.

- The voltage output $V_s(t)$, which is measured as a voltage drop across the resistor R_r, is proportional to the rate of change of the measured current given by Equation 18.

$$M = \mu_0 nS \hspace{4cm} \text{Equation 17}$$

$$V_s(t) = -M \frac{di_p(t)}{dt}, \hspace{3cm} \text{Equation 18}$$

where $i_p(t)$ is the measured current, $V_s(t)$ is the proportional differential voltage of the Rogowski coil, and M is the mutual inductance from Equation 17. The output voltage of the coil is proportional to the observed current. The L/R time constant $\tau \sim 1\mu s$, is significantly longer than

37

the current pulse being measured, this leads to a simplified version of Equation 14 producing

Equation 15

$$V_s = \frac{i_p(t)}{n} R_R,$$

Equation 19

where V_s is the voltage across the resistor R_R, n is the number of turns, and $i_p(t)$ is the measured

current [24].

4.9 Voltage Diagnostics

D-dot probes were used to measure both the voltage at the load, the load being the compact

MDO under test, and the voltage of the PFL. The first D-dot probe was place upstream of the oil

gap switch to measure the voltage on the PFL. The second was placed downstream of the oil gap

switch before the connected compact MDO and is used to measure the load voltage driving it.

The two D-dot probes are modified N-type connectors and are attached directly onto the outer

conductor of the coaxial transmission line. The sensors can be seen in Figure 4-10.

Figure 4-10: Photograph of the D-dot sensor input on outer conductor of coaxial transmission line.

D-dot voltage sensors are used to measure high voltage and are based on the electric field coupling principle. Prior calibration of the D-dot probes [25] were calculated to be 3.4×10^{-13} V^{-1} for the PFL and 3.74×10^{-13} V^{-1} for the transmission line post oil gap a switch. In Figure 4-11 the voltage pulse received from the D-dot sensors is shown as well as the integration of the same pulse. Both signals were numerically integrated following each test shot. Both the current and the voltage were recorded on a Tektronix DPO 7054 oscilloscope.
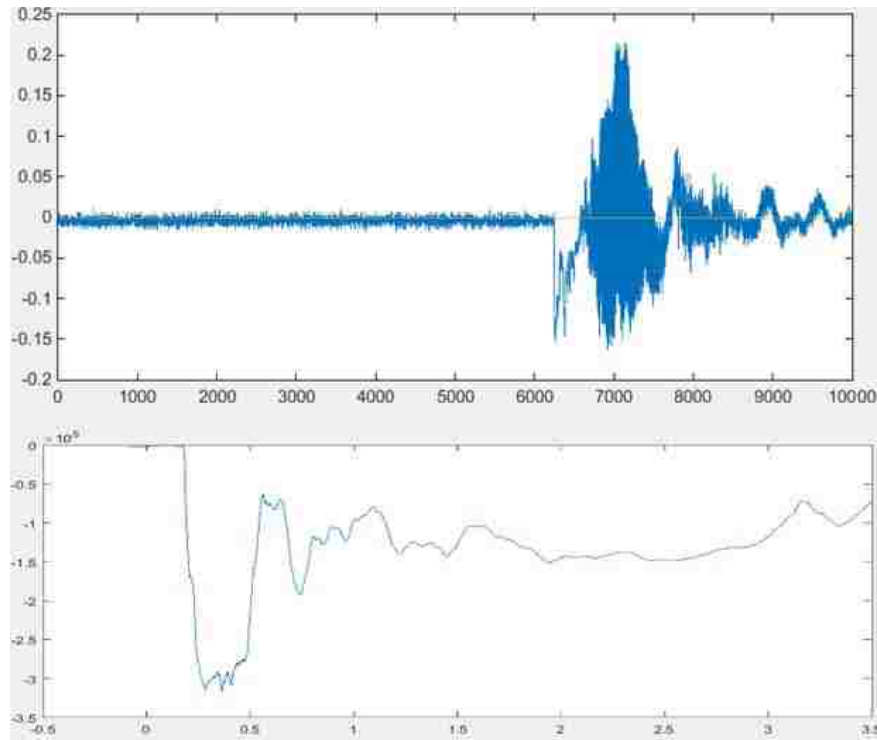
Figure 4-11: Measured voltage pulse and integrated waveform.

4.10 RF Diagnostics

The microwave pulse produced from the compact MDO was captured by a D-band rectangular waveguide. Shown below in Figure 4-12, the rectangular waveguide censor was placed in front of the cylindrical horn antenna at a distance 70 cm. This correlates to the far-field for the radiated microwave pulse.

Figure 4-12: Photograph of the rectangular waveguide sensor in front of the cylindrical horn antenna.

The signal was coupled out of an RG-241 cable and displayed on a Tektronix DPO 71254C oscilloscope in the screen room. Immediately following each test shot an FFT was applied in order to determine the frequency of the microwave pulse and, therefore, judge the compact MDO's performance. Simulations show that the π-mode frequency was 2.5 GHz, which corresponds to the TE_{11} output. This will be discussed further in the next chapter. A second RF diagnostic used to measure the shape of the produced microwave pulse was a neon bulb array shown in Figure 4-13. The board consist of 1,994 low-voltage neon bulbs arranged in a grid on a black Styrofoam base. When the produce microwave pulse is incident on the neon bulb array, the bulbs light up displaying the mode pattern of the microwave pulse. The pattern was captured using a long exposure DSLR camera.

Figure 4-13: Photograph of the neon bulb array used for mode characterization.

Chapter 5: Experimental Results

5. Experimental Results

Results from the experimental verification of the compact MDO tested on the PULSERAD accelerator are outlined in this Chapter. The information received on the voltage, current, and RF diagnostics were compared with simulation results for comparable input voltages. The PULSERAD accelerator typically operates with a voltage rise time of 4 ns and a pulse width of 30 ns. Therefore, the simulations of voltage rise times of 8 ns and 16 ns, as well as voltage pulse widths of 100 ns could not be experimentally verified using the PULSERAD accelerator at UNM and are intended to serve as a reference for the team at the NSWCDD Laboratory where the compact MDO is assembled on their variable pulse length and rep rate modulator. A basic outline of the NSWCDD accelerator will be presented in Section 5.4. In addition to voltage, current diagnostics, and RF output diagnostics, the mode radiated from the cylindrical horn antenna was also verified using two techniques. Wave forms from the voltage diagnostics, current diagnostics, and the D-band waveguide were collected and analyzed in the screen room of the laboratory immediately following each shot. Occasionally the PULSERAD fires prematurely, triggering all of the scopes before it can be collected and analyzed. Therefore, some of the data was not fully recorded. The power radiated from the antenna was not captured and characterized as the calorimeter, used in previous experiments to measure power, was in need of repair. Although the power data was not captured the simulations and experimental results relatively agree that ideal operation exists when the input voltage of the compact MDO is between a range of 300-320 kV. At these voltages, a steady π-mode frequency of 2.5 GHz was recorded.

5.1 Experimental Results

A voltage scan of input voltages between 285 kV and 340 kV was performed in order to compare the results of the simulations with the experimental data. A complete table outlining the results as well as the FFTs of the corresponding shots can be found in Appendix B. To summarize the results and illustrate the point of ideal input parameters compared to less than ideal operational parameters, the FFT of the emitted microwave pulse as a function of the load voltage is shown below.

As shown in Figure 5-1, the load voltage is just below the threshold shown in simulation results for effective operation. The result shown earlier in Figure 4-29 showed that mode competition exists between the π-mode frequency of 2.54 GHz and the $4\pi/3$ mode frequency of 2.79 GHz, with the $4\pi/3$ mode frequency being dominant.
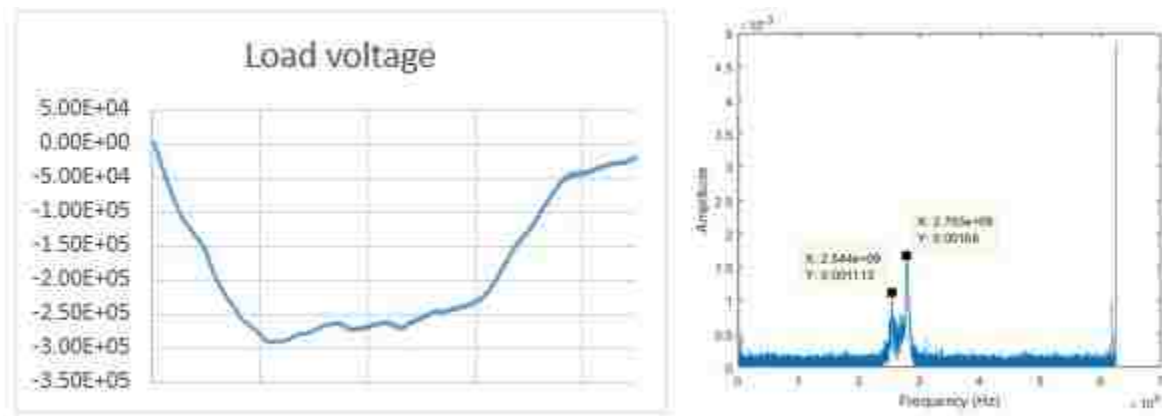
Figure 5-1: Load voltage below threshold and corresponding FFT of the microwave pulse.

Figure 5-2 shows the same case for the mode competition when the load voltage is less than ideal, in this case less than 300 kV. Figure 5-31 shows mode competition between the two modes with the π-mode frequency being dominant.
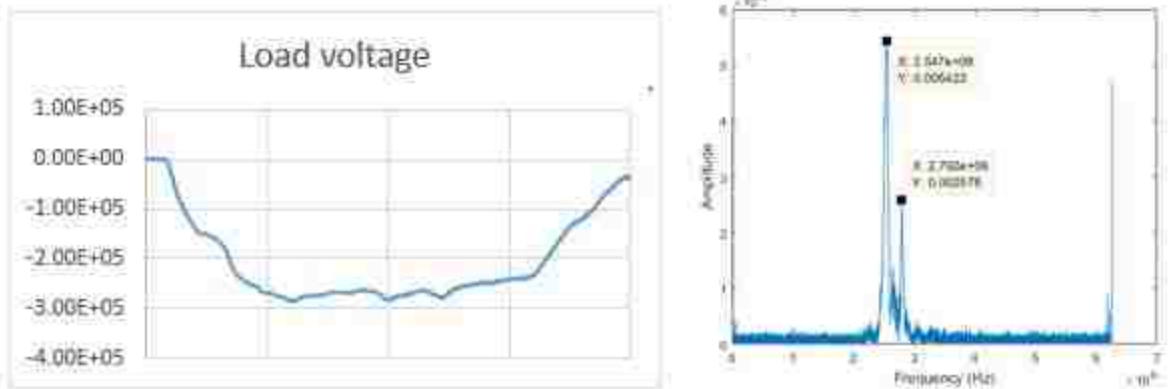
Figure 5-2: Load voltage at threshold of operation and corresponding FFT of microwave showing mode competition.

Figure 5-3 shows the load voltage at ~325 kV, and Figure 5-32 shows the FFT of the

produced microwave as a stable 2.54 GHz frequency with no mode competition from the $4\pi/3$
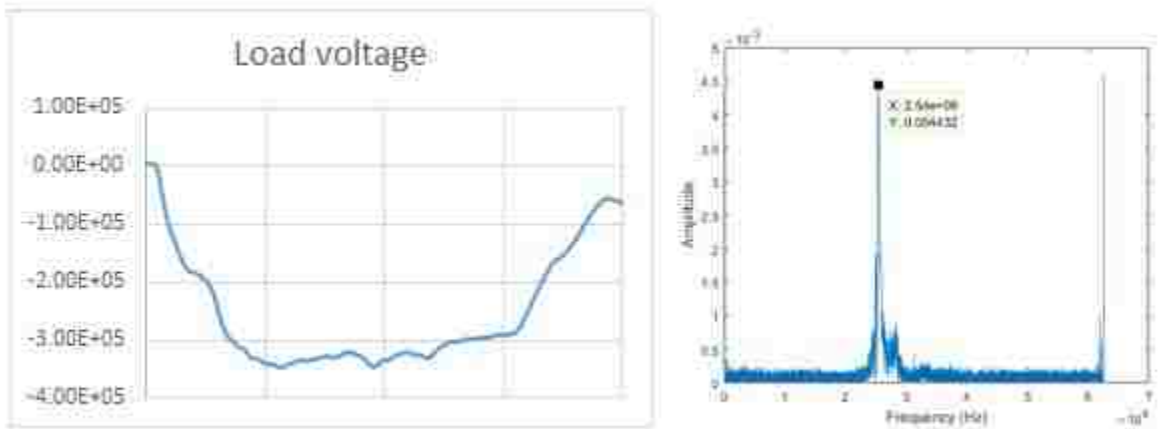
mode.

Figure 5-3: Load voltage within area of operation and corresponding FFT of microwave pulse showing no mode competition.

Figure 5-4 shows the typical waveform of the emitted microwave pulse with a pulse width of

~40 ns and a frequency of 2.53 GHz.
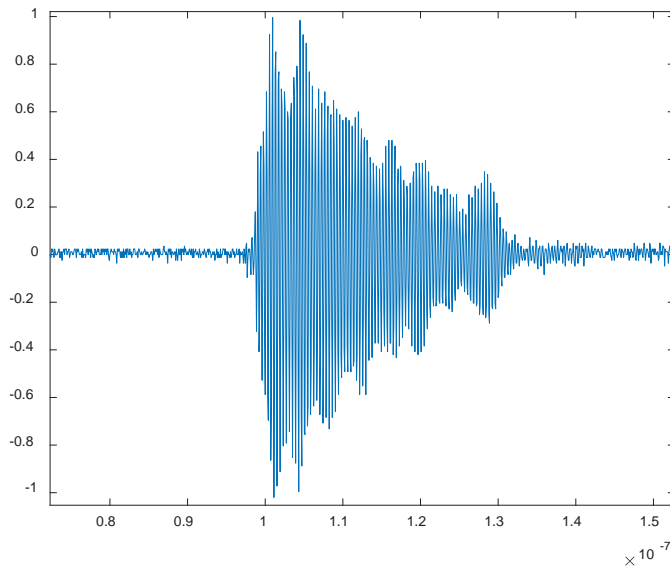
Figure 5-4: Typical microwave waveform.

The experimental results roughly match the simulation results in terms of ideal operation of the compact MDO being within a range of 300 kV to 320 kV. An explanation for the slight discrepancy between the two is due to the nature of simulations. In the simulations the entire system is in a perfect vacuum, in a stable environment with the input voltage being perfectly defined, and all components of the system in perfect alignment. In experimental conditions, great care is taken to maintain vacuum and assemble all of the components of the system in perfect alignment. The voltage wave form and magnitude are variable and depend on several different components of the system including the pressure of SF_6 in the Marx switches, charging voltage of the Marx, and distance of the oil gap switch. As stated in [28], agreement between simulation and experiment is good when: (1) the simulation reproduces the qualitative behavior of the experiment, i.e. changing parameter "A" produces a similar change in parameter "B" in both simulations and experiment, and (2) when the steady-state values of measured quantities agree with simulation results to within the error of the measurement. In Figure 5-5 the

experimental normalized RF amplitudes are plotted against the corresponding measured load

voltages as well as the simulated RF power of the simulations plotted against the applied voltage

of the system. The results from the plots show that there is general correspondence between the

simulations and the experimental data with regard to the RF output and the applied voltage to the

system, satisfying the conditions for (1) mentioned above.
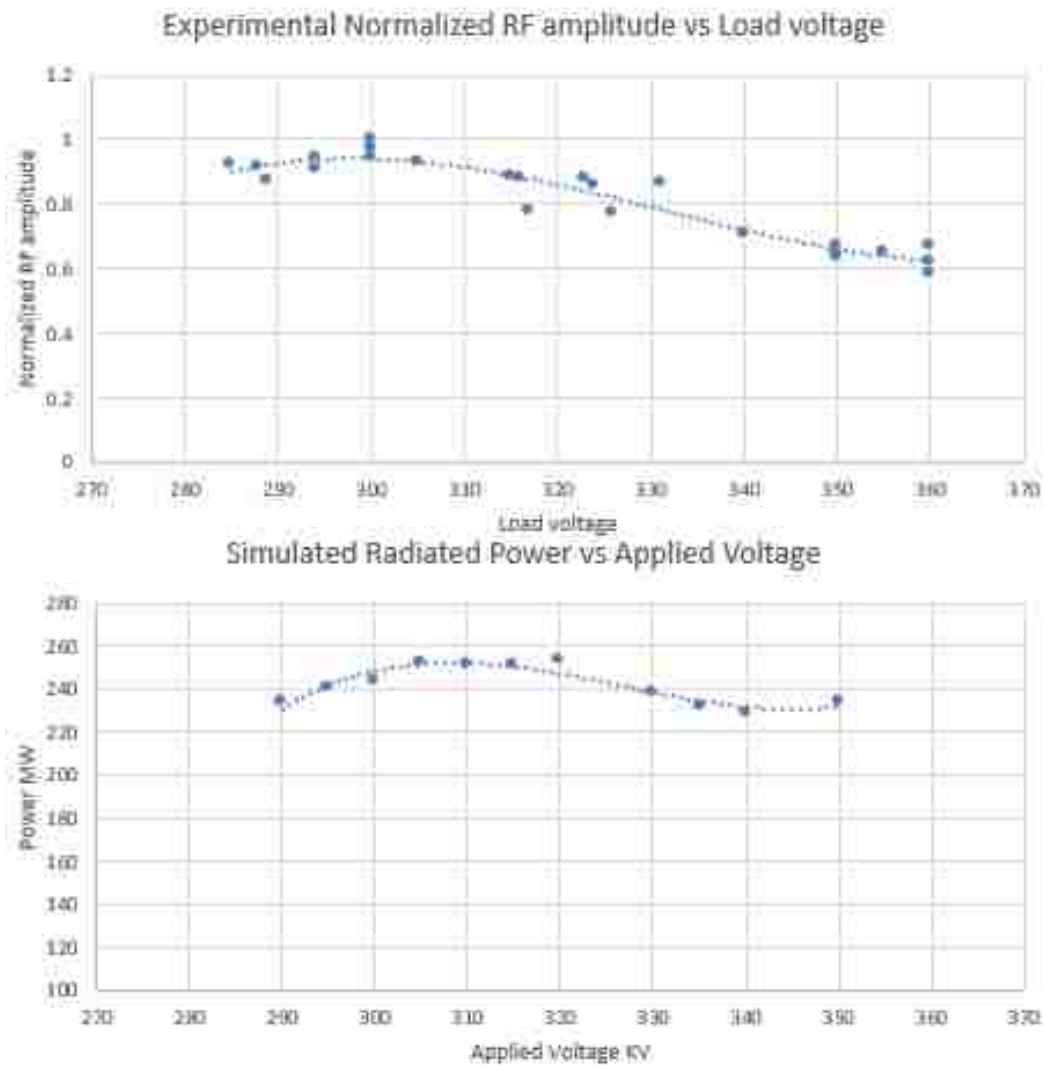
Figure 5-5: Normalized measured RF amplitude vs measured load voltage (top) and simulated RF power in simulations vs, applied voltage (bottom)

45

5.2 Mode Verification

In addition to the FFT of the radiated field, a second verification of compact MDO performance is the verification of the mode propagating out of the antenna. This was accomplished two different ways. First using the neon bulb array, described in 4.4.3, and second the D-band rectangular waveguide, which was positioned at different places along the relative X and Y axis to measure power at each position. The thought behind the second procedure was that if the microwaves radiated from the cylindrical antenna were Gaussian, the power would be relatively more powerful and the center i.e. (0,0) and then have a relatively equal decrease of power in the plus and minus X and Y directions. The results of radiating the neon board and capturing the image using a long exposure DSLR camera is shown in Figure 5-6.
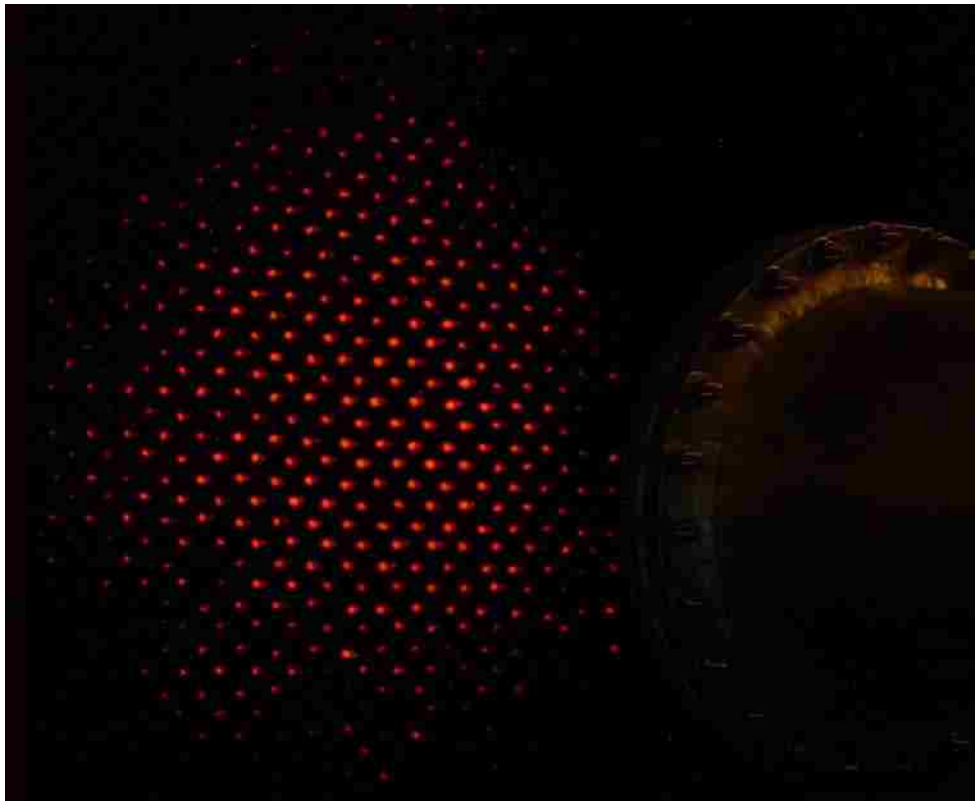
Figure 5-6: Result of radiating neon board.

The intensity of the neon bulbs on the board is highest in the center of the board and towards the edge of the illuminated neon grid the lit bulbs are not as intense. One note is that the beam is not perfectly circular and appears to be rotated according as seen on the neon grid. The results from placing the D-band waveguide at different locations is shown in Figure 5-7. The anticipated behavior of the relative decrease of intensity from the center in the plus and minus X and Y directions is observed.
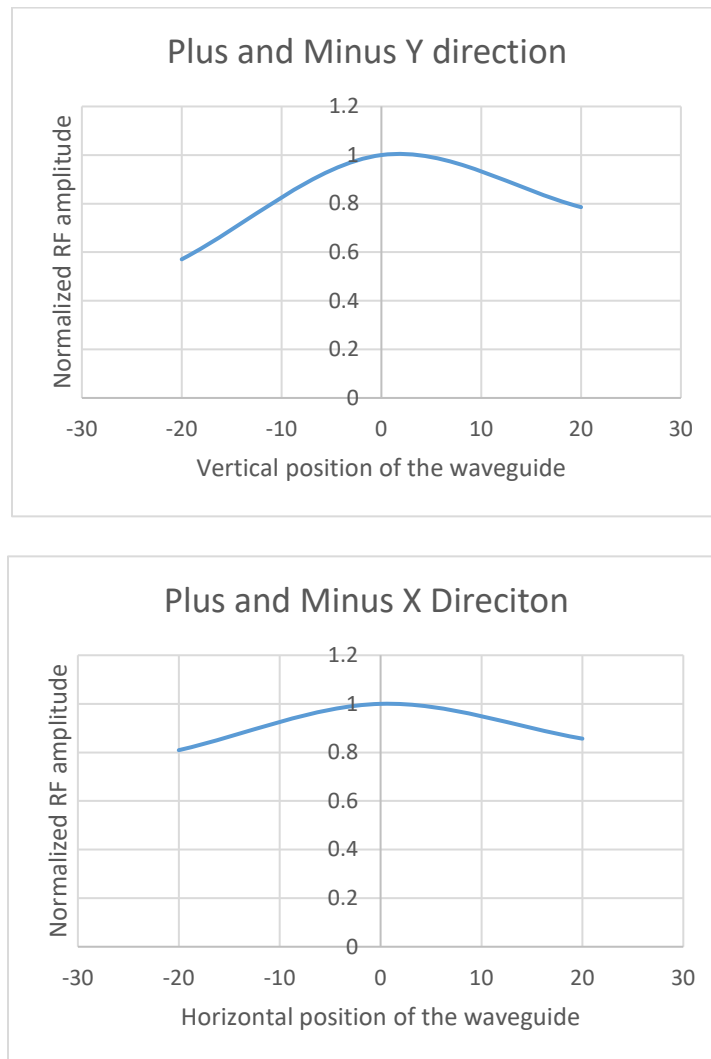
Figure 5-7: Measured normalized RF amplitude moving waveguide in +/- X direction (top) and in +/- Y direction (bottom).

.

5.3 NSWCDD Set-up

Following magnetron characterization at UNM, the compact MDO and permanent magnet, as well as its supporting components were re-assembled and tested in the Naval Surface Warfare Center Dahlgren Division (NSWCDD) High Voltage Advanced Research (HIVAR) Laboratory in Dahlgren, Virginia. The pulsed power system used to drive the magnetron is a 15-stage modulator comprised of linear transformer drivers (LTDs). Unlike the single shot accelerator used at UNM, the NSWC modulator is capable of firing a burst of pulses up to 10 shots at 10 Hz. Figure 5-8 shows the NSWC's modulator below.
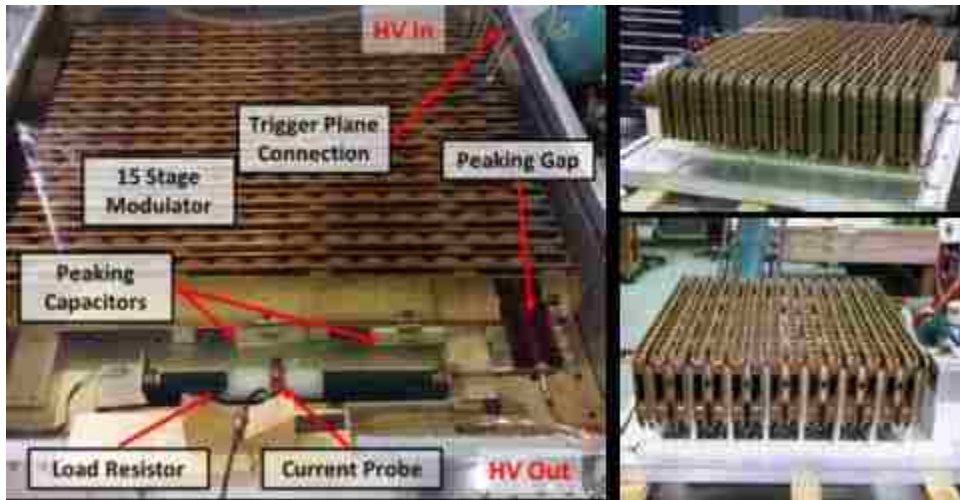
Figure 5-8: NSWCDD's modulator used to test the UNM compact MDO.

The output of the modulator was connected to a shaping flange with an integrated V-dot, peaking gap with an impedance matching section and a custom made oil/vacuum interface. The remaining hardware downstream of this point is the same that was used in the magnetron characterization at UNM, i.e. vacuum chamber, Rogowski coils, compact MDO with permanent magnet, beam dump, and conical horn antenna. Figure 5-9 shows the fully assembled test set-up.
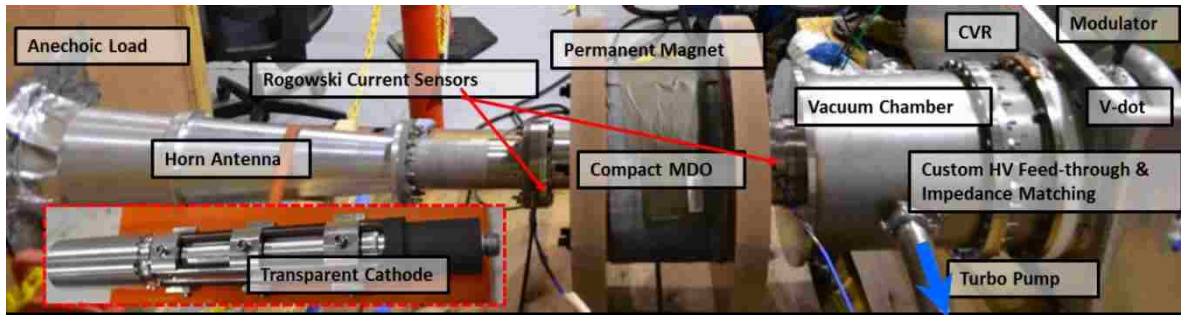
Figure 5-9: Final assembly of permanent magnet on the NSWC modulator.

From the characterization of the magnetron at UNM, the output of the NSWCDD modulator produced an ~300 kV, 15 kA pulse into the magnetron which has a load resistance of ~20 Ω. Per UNM's operational recommendations, NSWC's modulator was reconfigured to provide a pulse width between 50-60 ns. Although the PULSERAD accelerator is not able to produce pulses of this length, simulations had shown that there is a strong correlation between longer pulse widths and mode competition. It was recommended that the pulse width be less than 100 ns and closest to the pulse width of the PULSERAD as possible. When operation was changed form single shot to burst mode, no significant changes of the output waveforms were observed. Figure 5-10 shows the waveform for signal when the system was operated in burst mode. The output waveforms show an envelope of more than 30 ns and an output frequency of 2.5 GHz, matching the results from both simulation and experimental testing with the PULSERAD accelerator. Figure 5-11 shows the input current and leakage current recorded by the Rogowski coils.
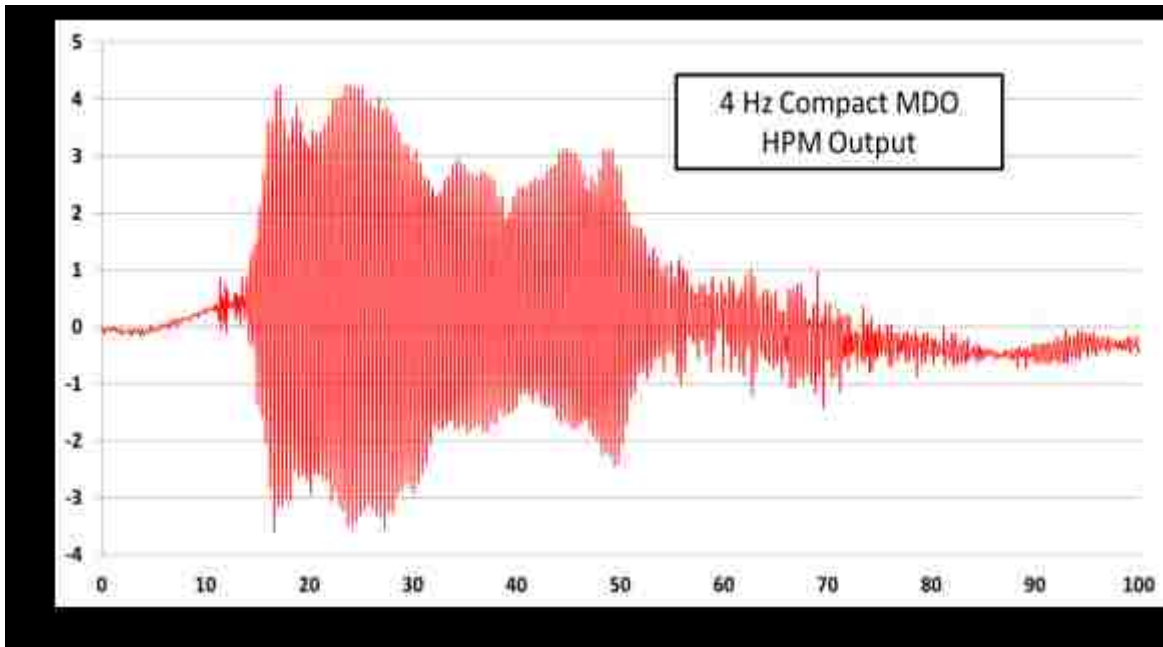
Figure 5-10: Typical microwave waveform when modulator operates in burst mode.
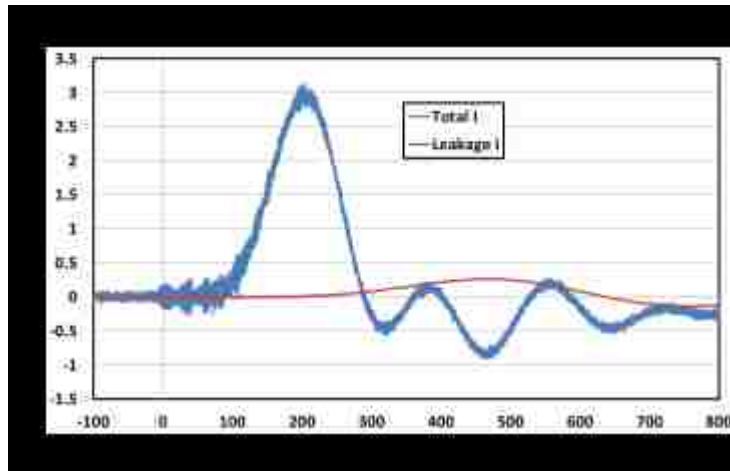
Figure 5-11: Measured input current and leakage current.

Chapter 6: Conclusions

6. Experimental Results

The scope of work completed for this thesis project includes performing simulations, assembling the permanent magnet and compact MDO, testing the compact MDO using the PULSERAD accelerator, and finally assembling and testing the compact MDO on the NSWCDD modulator. The simulation process properly defined ideal operating parameters, i.e. input voltage, pulse width, and voltage rise time, to achieve the maximum power radiated axially out of the compact MDO. The permanent magnet was carefully assembled over the compact MDO in the laboratory at UNM. This paid tremendous dividends months later when the permanent magnet was unpackaged and assembled in Dahlgren, Virginia at the NSWCDD pulsed power and microwaves facility. Testing the compact MDO with permanent magnet with the PULSERAD accelerator confirmed how well the simulation results of ideal operational parameters really matched the experiment. This information was passed to the NSWCDD microwaves group in order to replicate the experiment using their pulsed power system. The permanent magnet compact MDO was assembled at the NSWCDD microwaves facility in October 2017 and operation was experimentally verified in December 2017.

6.1 Process Improvements

Through the progression of completing this thesis project, I would like to provide some feedback on the process and how I think it can be improved for future students working in the Pulsed Power, Beams, and Microwaves Laboratory. I believe this is important to note and will be beneficial to future students working with the PULSERAD accelerator and in the laboratory in general. First off, there should be a plan implemented for routine maintenance and cleaning of

the Marx Bank, PFL, and oil gap switch. There can be a significant amount of downtime mid-experiment for addressing these issues when the accelerator is not working properly. Much of this downtime can be avoided with routine monthly or quarterly maintenance schedules. Secondly, the data acquisition system could be upgraded to a more robust and automated system. Currently the process for collecting data involves saving waveforms to USB drives and transferring them to a computer in the control room, integrating the D-dot waveforms by hand using an Excel spreadsheet, and saving the waveforms in a folder using a naming convention. This leaves a lot of opportunity for human error in both data collection and data management. Towards the end of the experiment a LabVIEW program was installed to do address this issue. This is a very good first step, but it would be very beneficial to continually upgrade and create new versions of this program. Another benefit to an automated data collection process would be the prevention of lost data. There were several occasions when the Marx bank would "pre-fire," causing the scopes to trigger and the data would be lost before it was properly recorded and analyzed. Some extra engineering controls and work planning, including a maintenance schedule, would be a tremendous benefit for the future students doing experiment in the laboratory.

6.2 Future Work

The preceding simulations and experimental results are part of a much broader effort by the NSWCDD to ultimately design a full MDO with a virtual cathode for testing. The full MDO as described by Fuks and Schamiloglu is estimated to have an electrical efficiency of 70% [13]. The MDO with virtual cathode would completely eliminate a physical cathode from the interaction area. Several advantages to having a cathodeless system include: robustness of the

system, and immunity form electron bombardment, pulse shortening, decreasing electron efficiency, and frequency shift [29].

Work is also being done at UNM exploring alternative magnet geometries. One shortcoming of the current permanent magnet compact MDO is that it requires a very large and very expensive permanent magnet to maintain the 0.33T magnetic field within the interaction area. Simulations are ongoing for alternative magnet geometries and unique magnetic field solutions. One prospective solution is inserting 6 individual permanent magnet cylinders into each of the vanes within the anode block. This may provide the necessary magnetic field for operation and would significantly reduce the size and weight of the total system.

7. Appendix A: Simulation Results

Charge Voltage (kV)	Rise Time (ns)	Pulse Length (ns)	Anode Current (kA)	Leakage Current (kA)	Microwave Power (MW)	Microwave Frequency (GHz)
285	4	30	6.31	1.81	188.98	2.5/2.76
		100	6.4	1.85	188.98	2.52/2.77
	8	30	6.34	1.83	44.9	2.76/2.5
		100	6.4	1.85	45	2.77/2.5
	16	30	6.39	1.84	44.74	2.77/2.5
		100	6.31	1.85	43.8	2.77
290	4	30	5.58	1.86	237.09	2.5
		100	6.33	1.85	188.98	2.52/2.77
	8	30	5.4	1.84	238.58	2.5
		100	6.64	1.87	238.58	2.51/2.77
	16	30	6.56	1.87	45.31	2.76
		100	6.62	1.88	46.65	2.77
295	4	30	5.7	1.9	245.41	2.5
		100	6.68	1.92	245.41	2.5/2.77
	8	30	5.68	1.85	240.85	2.5
		100	6.78	1.9	240.85	2.51/2.77
	16	30	6.75	1.91	48	2.77/2.53
		100	6.78	1.91	48.55	2.77
300	4	30	6.26	1.8	188.98	2.5
		100	6.96	1.94	240.75	2.52/2.77

	8	30	5.88	1.95	243.56	2.5
		100	6.93	1.95	243.56	2.5/2.77
	16	30	6.9	1.95	48.56	2.77/2.5
		100	6.91	1.95	48.55	2.77
305	4	30	5.93	1.89	254	2.5
		100	7.06	1.98	255	2.5/2.77
	8	30	6.18	1.92	252	2.5
		100	7.15	1.98	252	2.52/2.77
	16	30	7.02	1.97	117	2.53/2.8
		100	7.04	1.98	117.85	2.77/2.52
310	4	30	6.37	1.94	253	2.5
		100	7.27	2.01	253.65	2.52
	8	30	6.31	1.98	251.49	2.5
		100	7.3	2.01	251.49	2.52/2.77
	16	30	7.28	2.02	52.07	2.77
		100	7.28	2.03	52.09	2.77
315	4	30	6.65	2.04	250.55	2.5
		100	7.41	2.05	250.55	2.52/2.77
	8	30	6.63	1.99	250.6	2.5
		100	7.44	2.07	250.6	2.52/2.77
	16	30	7.46	2.05	54.97	2.77
		100	7.49	2.05	54.97	2.77
320	4	30	6.92	2	255.77	2.5
		100	7.67	2.1	255.77	2.52/2.77
	8	30	6.65	2	252.43	2.5

		100	7.72	2.09	252.43	2.52/2.77
	16	30	7.5	2.1	94	2.53/2.77
		100	7.67	2.1	94.26	2.77/2.52
325	4	30	7.45	2.19	109.27	2.533
		100	7.67	2.16	109.27	2.77/2.54
	8	30	7.54	2.12	133.24	2.53/2.77
		100	7.68	2.13	133.24	2.76/2.54
	16	30	7.82	2.13	54.09	2.77
		100	7.72	2.14	53.6	2.77
330	4	30	7.23	2.07	254.14	2.533
		100	7.6	2.15	254.24	2.52
	8	30	7.2	2.06	253.18	2.533
		100	7.65	2.16	253.18	2.52
	16	30	7.97	2.17	53.89	2.77
		100	7.84	2.15	57	2.76
335	4	30	7.36	2.07	254.41	2.53
		100	7.68	2.11	253.86	2.52
	8	30	7.51	2.1	249.94	2.53
		100	8.24	2.15	251.11	2.52
	16	30	8.18	2.12	2.89	2.77
		100	8.06	2.18	55.75	2.76
340	4	30	7.9	2.14	248.62	2.53
		100	10.09	2.12	251.51	2.52
	8	30	7.74	2.14	248.55	2.53
		100	7.81	2.12	245.21	2.52

	16	30	8.33	2.21	137.24	2.53/2.77
		100	8.41	2.21	54.68	2.76
345	4	30	8.06	2.15	245.9	2.533
		100	10.38	2.15	245.9	2.52
	8	30	10.46	2.16	63.53	2.53/4
		100	10.51	2.15	63.53	2.55/3.99
	16	30	8.66	2.27	50.46	2.77
		100	8.65	2.24	50.47	2.77
350	4	30	10.54	2.21	34.69	4.33/2.53/4/2.77
		100	10.77	2.18	242.32	2.52
	8	30	8.41	2.18	243.05	2.533
		100	10.76	2.18	244.93	2.528.
	16	30	8.69	2.3	51.04	2.77
		100	8.77	2.26	20.7	2.75

8. Appendix B: Experimental Results

Shot	Input Current (kA)	Leakage Current (A)	Mean Load Voltage (kV)	Voltage Rise Time (ns)	Pulse Width (ns)	Frequency (GHz)
1	N/A	N/A	246	7.6	30.96	2.74
2	N/A	N/A	304	7.28	31.52	2.53/2.73
3	N/A	N/A	291	5.84	30.8	2.54/2.74
4	N/A	N/A	312	7.28	30.48	2.54
5	N/A	N/A	308	5.84	30.88	2.54
6	N/A	N/A	312	6.48	30.56	2.54
7	N/A	N/A	295	5.84	31.12	2.54
8	5.928	0.3926	296	6.24	30.48	2.54
9	7.8	0.4784	321	5.92	30.48	2.54
10	7.384	0.4498	316	5.76	30.88	2.54
11	7.176	0.4576	308	6.4	30.72	2.54
12	6.552	0.4368	224	10.4	30	2.53
13	7.02	0.4576	308	6.48	30.4	2.54
14	N/A	N/A	311	6.24	30.8	2.54
15	6.604	0.429	297	6	30.72	2.53
16	6.5	0.4004	298	5.84	31.04	2.53
17	6.5	0.3926	298	7.04	30.08	2.53
18	7.332	0.4576	312	6.56	30.56	2.54
19	7.436	0.4758	315	5.68	30.88	2.55
20	6.812	0.4394	301	6.96	30.96	2.54
21	7.54	0.4576	316	7.04	30.88	2.54
22	8.164	0.468	325	6.08	31.12	2.54
23	8.164	0.4862	326	6.48	30.96	2.54
24	6.188	0.442	297	6.32	30.88	2.53
25	8.788	0.468	338	6.08	30.64	2.55
26	7.124	0.468	312	5.76	31.04	2.54
27	8.58	0.4758	336	6.24	31.2	2.55
28	7.852	0.494	328	5.92	30.88	2.55
29	6.812	0.4394	312	5.84	30.48	2.54
30	7.644	0.4758	314	6.48	31.2	2.54
31	7.436	0.4758	322	5.68	30.88	2.54
32	6.292	0.429	294	6.24	30.96	2.53
33	6.084	0.4004	288	7.12	30.96	2.53
34	8.164	0.4758	324	7.12	30.56	2.54
35	7.228	0.4576	311	6.56	30.56	2.54

9. References

[1] J. Benford, J. Swegle and E. Schamiloglu, High Power Microwaves, 3rd Ed., Boca Raton, FL: CRC Press Taylor & Francis Group, LLC, 2016.

[2] J.E. Brittain, "Electrical Engineering Hall of Fame Albert W. Hull," *Proceeding of the IEEE,* vol. 98, no. 4, pp. 635-637, April 2010.

[3] A.W. Hull, "The Magnetron," *Journal of the American Institute of Electrical Engineers,* vol. XL, no. 9, 1921.

[4] H.A.H. Boot and J.T. Randall, "The Cavity Magnetron," *IEEE Proc. Radiolocation Conf.*, pp. 928, 1946.

[5] S. Phelps, The Tizard Mission: The Top Secret Operation that Changed the course of World War II, Yardley, PA: Westholme Publishing, 2010.

[6] A. Palevsky and G. Bekefi, "Microwave Emission from Pulsed, Relativistic E-beam Diodes," *Phys. Fluids,* vol. 22, p. 986, 1979.

[7] 2012. [Online]. Available: http://www.boeing.com/Features/2012/10/bds_champ_10_22_12.html.

[8] M. Fuks and E. Schamiloglu, "Rapid Start of Oscillations in a Magnetron with a "Transparent" Cathode," *Physical Review Letters,* vol. 95, p. 205101, 2005.

[9] H. Bosman, M. Fuks, S. Prasad and E. Schamiloglu, "Improvement of the Output Characteristics of Magnetrons Using the Transparent Cathode," *IEEE Transactions on Plasma Science,* vol. 34, no. 3, pp. 606-619, June, 2006.

[10] M. Fuks, N. Kovalev, A. Andreev and E. Schamiloglu, "Mode conversion in a Magnetron With Axial Extraction of Radiation," *IEEE Transactions on Plasma Science,* vol. 34, no. 3, pp. 620-626, 2006.

[11] S. Prasad, M. Roybal, C. Buchenauer, K. Prestwich, M. Fuks and E. Schamiloglu, "Experimental Verification of the Advantages of the Transparent Cathode in a Short-Pulse Magnetron," *Proceedings of the 17th IEEE International Pulsed Power Conference*, Washington, DC, 29 June - 02 July, 2009, p. 81.

[12] M. Fuks and E. Schamiloglu, "High Efficiency Relativistic Magnetron Wtih Diffraction Output," *Proceedings of the 17th IEEE International Pulsed Power Conference*, Washington, DC, 29 June - 02 July, 2009, p. 74.

[13] M. Fuks and E. Schamiloglu, "70% Efficient Relativistic Magnetron With Axial Extraction of Radiation Through a Horn Antenna," *IEEE Transactions on Plasma Science,* vol. 38, no. 6, pp. 1302-1312, 2010.

[14] C. Leach, S. Prasad, M. Fuks and E. Schamiloglu, "Suppression of Leakage Current in a Relativistic Magnetron Using a Novel Design Cathode Endcap," *IEEE Transactions on Plasma Science,* vol. 40, no. 8, pp. 2089-2093, 2012.

[15] C. Leach, S. Prasad, M. Fuks and E. Schamiloglu, "Compact Relativistic Magnetron with Gaussian Radiation Pattern," *IEEE Transaction on Plasma Science,* vol. 40, no. 11, pp. 3116-3120, 2012.

[16] C. Leach, S. Prasad, M. Fuks and E. Schamiloglu, "Compact A6 Magnetron with Permanent Magnet," *Proceedings 2012 IEEE International Vacuum Electronics Conference*, Monterey, CA, 24-26 April, 2012, p. 491-492.

[17] L. Tianming, L. Jiayin and H. Biao, "Experimental Studies on the A6 Relativistic Magnetron Wtih Permanent Magnet," *IEEE Transactions on Plasma Science,* vol. 39, no. No. 9, pp. 1776-1780, September 2011.

[18] A. Levin and A. Sayapin, "Relativistic Magnetron With Inbuilt Magnetic Block," *Proceedings EUROEM 2012*, Toulouse, France, 02-06 July, 2012, p. 252.

[19] "Poisson Superfish," Los Alamos Accelerator Code Group, [Online]. Available: http://laacg.lanl.gov/laacg/services/download_sf.phtml. [Accessed 03 03 2018].

[20] J. Collins, Microwave Magnetrons, New York: McGraw-Hill, 1948.

[21] M. Jones, "Cathode Priming of a Relativistic Magnetron Using Multiple Emission Zones on Projection Ablation Lithography Cathode," Ph.D. Dissertation, Department of Nuclear and Radiological Sciences, University of Michigan, Ann Arbor, MI, 2005.

[22] V. Neculaes, "Magnetron Magnetic Priming for Rapid Startup and Noise Reduction," Ph.D. Dissertation, Department of Nuclear and Radiological Sciences, University of Michigan, Ann Arbor, MI, 2005.

[23] "MAGIC Tool Suite," 8th May 2017. [Online]. Available: http://www.orbitalatk.com/magic/description.aspx.

[24] S. Prasad, "Fast Start of Oscillations in a Short-Pulse Relativistic Magnetron Driven By a Transparent Cathode," Ph.D. Dissertation, University of New Mexico, Albuquerque, NM, 2010.

[25] C. Leach, "High Efficiency Axial Diffraction Output Schemes for the A6 Relativistic Magnetron with Modified Output Configuration," Ph.D. Dissertation, University of New Mexico, Albuquerque, NM, 2014.

[26] J. McConaha, "Experimental Verification of the Concept of the Relativistic Magnetron with Simple Mode Converter," M.S. Thesis, University of New Mexico, Albuquerque, NM, 2016.

[27] C. A. Balanis, Antenna Theory Analysis and Design Fourth Edition, Hoboken, New Jersey: John Wiley & Sons Inc., 2016.

[28] R. Barker and E. Schamiloglu, High-Power Microwave Sources and Technologies, Piscataway, NJ: IEEE Press, 2001.

[29] M. Fuks, S. Prasad and E. Schamiloglu, "Efficient Magnetron With a Virtual Cathode," *IEEE Transactions on Plasma Science,* vol. 44, no. 8, pp. 1298-1302, August 2016.

[30] "Efficient Magnetron With a Virtual Cathode," *IEEE Transactions on Plasma Science,* 2016.

[31] I. Metwally, "Design of Differnt Self-Integrating and Differentiating Rogowski Coils for Measuring Large-Magnitude Fast Impulse Currents," *IEEE Transactions on Instrumentation and Measurement,* vol. 62, no. 8, pp. 2303-2313, 2013.

[32] M. Fuks, S. Prasad and E. Schamiloglu, "Increased Efficiency and Faster Turn-on in Magnetrons using the Transparent Cathode," *Proceedings CAVMAG2010*, Bournemouth, UK, 19-20 April, 2010, p. 76-81.

[33] S. Prasad, C. Leach, K. Prestwich, C. Buchenauer, M. Fuks and E. Schamiloglu, "Experimental Demonstrations fo the Output Characteristics of the A6 Magnetron on PULSERAD 110a, a Very Short Risetime Accelerator at UNM," *Proceedings 2012 IEEE International Vacuum Electronics Conference*, Monterey, CA, 24-26 April, 2012, p. 491-492.

[34] E. Schamiloglu and M. Fuks, "Rapid start of oscillations in a magnetron with a "transparent" cathode," *Phys. Rev. Lett. 95, 205101,* 2005.

[35] E. Schamiloglu and M. Fuks, "The Transparent Cathode: Rejuvenator of Magnetrons and Inspiration for New RF Sources," *Proceedings of the IET Conference on High Power RF Technologies,* London, UK, February 2009, p. O1.2.